Lisa Sletten

Coherence Based Imaging in Echocardiography Using a 2D Matrix Array Probe

A Pilot Study on the Performance of the 2D Coherence Factor Compared to the DAS Algorithm

NTNU
Norwegian University of
Science and Technology

Lisa Sletten

Coherence Based Imaging in Echocardiography Using a 2D Matrix Array Probe

A Pilot Study on the Performance of the 2D Coherence Factor Compared to the DAS Algorithm

Master's thesis in Electronics System Design and Innovation
Supervisor: Svein-Erik Måsøy
June 2020

Norwegian University of Science and Technology
Faculty of Information Technology and Electrical Engineering
Department of Circulation and Medical Imaging

NTNU
Norwegian University of
Science and Technology

Foreword

This paper is the result of a master thesis completed at the Faculty of Information Technology and Electrical Engineering during the spring of 2020. The thesis is written at the Department of Circulation and Medical Imaging at NTNU. I would like to thank the department for supplying such interesting thesis themes, and for supplying clever supervisors and providing access to ultrasound equipment. I would like to thank the professors that have taught the ultrasound classes at the department, especially Jørgen Avdal and Hans Torp. The ultrasound classes have helped deepen my understanding of the field of ultrasound.

I would like to especially thank my supervisor Svein-Erik Måsøy for great explanations, chats and mentoring throughout the duration of the master project. I would also like to thank Ole Marius Hoel Rindal for providing help with USTB and also for running the code on the computers at UiO. Lastly, I would like to thank Ali Fatemi for helping me to understand the 2D Coherence Factor and its implementation in USTB.

Norwegian University of Science and Technology

Trondheim, June 2020

Lisa Sletten

Lisa Sletten

Abstract

An excellent ultrasound image resolution is important in securing high diagnostic value of echocardiograms. This paper is a pilot study on the performance of an ultrasound processing tool called the 2D Coherence Factor. The 2D Coherence Factor is an ultrasound signal processing tool that aims to reduce clutter in ultrasound images by use of an adaptive approach that exploits the coherence of an ultrasound signal. The aim of the thesis is to gauge the performance of this algorithm on a database of ultrasound patient data, and judge if the technique works best for aperture blockages in the elevation direction.

Over 2200 ultrasound images were processed using MATLAB code and videos were created from the images. These videos were then analyzed using a three step method. The first step was an analysis of the change in image quality compared to the same images processed with the delay-and-sum algorithm. The second step was to examine the type of aperture blockages and figure out if there was a connection between the change in image quality with the 2D CF and the nature of the aperture blockages. The third and final approach was to examine the videos in light of their quality, aperture blockage and also the type of image view that was used during acquisition.

The results indicate that the 2D Coherence Factor performs better when there is a blockage in elevation direction. Of the 43 videos that have some form of blockage in elevation direction, 68.12 % are deemed to have better image quality when the 2D Coherence Factor is applied. In addition, all 9 videos showcasing a blockage in elevation-only direction have better image quality when the 2D Coherence Factor is used. The results also indicate that the algorithm performs better for images with few blocked aperture elements. The images views that experienced the best image quality with the 2D CF were the views with the least amount of blocked elements on average. Furthermore, the videos that were improved by the 2D CF have a lower mean amount of blocked elements than the videos that show no significant improvement with the same technique.

The results in this pilot study are indicative of there being an increase in image quality for most of the videos in the study. Also, no videos had their video quality decreased by the 2D Coherence Factor. This algorithm therefore warrants further study.

Contents

List of Figures

List of Tables

1 Introduction

Cardiovascular disease (CVD) is the number one cause of death on a global basis [6]. This family of diseases takes an estimated 17.9 million lives annually [6]. There are a number of risk factors associated with cardiovascular diseases, obesity being one of them. The increase in obesity in the population means the prevalence of CVDs will most likely grow in the coming years. The World Health Organization estimates that the deaths caused by cardiovascular diseases could be as high as 24.2 million in 2030 [7]. In order to treat and prevent cardiovascular disease, accurate and effective diagnostic tools are crucial. Echocardiography is a very important use of diagnostic ultrasound, and is one of the most widely used tests within cardiology [8]. Echocardiography is in many cases the preferred diagnostic tool, as it is cost effective and non-intrusive. It is therefore problematic that the image quality of many ultrasound images is heavily reduced, yielding low or non-existing diagnostic value. Other, more intrusive procedures might then be chosen, such as MRI or another type of echocardiogram like the transesophageal echocardiogram.

Ultrasound technology is changing rapidly, and a number of attempts have been made to reduce the effect of reverberation clutter on image quality. Harmonic imaging (HI) is one such approach. Images utilizing the second harmonic and not the fundamental frequency are proven to have a reduction in image artefacts and noise as well as increased sidelobe suppression [1]. Harmonics are generated as the pulse travels through tissue on transmit, and the generation is the strongest along the beam axis. Reverberation echoes exhibit both low amplitude and coherency, and they therefore do not contribute significantly to the generation of harmonics [9]. Although effective, harmonic imaging does not yield significant improvement in all circumstances. A paper from 2004 compared harmonic imaging to fundamental imaging in the case of transthoracic echocardiography and found that HI decreased the number of patients with poor image quality from 62 to 33 [10].

A common approach within ultrasound research is to apply a novel adaptive beamforming technique to improve image quality. Techniques that seek to replace the simple delay-and-sum (DAS) beamformer are abundant. A number of these are so-called coherence based techniques. In 1994 Mallart and Fink formulated a way of calculating the Coherence Factor, or Focusing Criterion, which is the ratio of coherent energy across the transducer to

the incoherent energy [11]. Later, Li et. al published an extension of this in a paper on the Generalized Coherence Factor (GCF) [12]. The GCF can be defined as the ratio of energy resulting from directions close to the main beam to the total received energy from every direction. The Fourier Transform is used in the calculation of the GCF, which is not the case for the Coherence Factor. Lediju et al. [13] present the Short-Lag Spatial Coherence technique. The SLSC is calculated by taking the integral of the spatial coherence for a number M lags. This number M is intended to be small relative to the number of aperture elements, i.e the name short lag. The SLSC was applied to echocardiograms in [14] and found to decrease the amount of patients with poor-quality images from 21% to 7%. The clinical tests showed an increased visibility of endocardial borders and a reduction in clutter.

In [15], Camacho et al. exploit the phase as opposed to the amplitude of the coherence, in order to suppress both grating lobes and side lobes. The coherence ratio for the amplitude coherence technique is close to unity at the grating lobes, which reduces their suppression. However, the coherence ratio is not unity for the phase coherence factor, and it can therefore be used to suppress grating lobes. The Phase Coherence Factor uses the phase of the backscattered signals to weight the image.

The Coherence Factor proposed in [11] uses the whole aperture at once for the coherence calculations. Experiments by Fatemi et al. [4] show that common sources of reverberation noise, including blockages by the ribs and reflections from the lung cavity, can often lead to only parts of the aperture receiving the reverberations. In an attempt to exploit this fact, Fatemi et al. have developed a two dimensional coherence factor, the 2D Coherence Factor, that takes into account spatial variations of received energy across the aperture [3], and subsequently the local variations in coherence. The 2D Coherence Factor is calculated by using a sliding window of a given number of rows across the elevation direction of the transducer array. Dividing the array into smaller subsections can uncover spatial variations in the backscattered reverberations, and lead to a more precise coherence technique that is more sensitive to local variations in the coherence.

This novel technique has not yet been tested on larger amounts of data. This paper seeks to apply the 2D Coherence Factor to a database of high quality data from real patients, and try to establish whether there is an improvement in image quality. The paper also

looks to establish if there is any relationship between the type of aperture blockages and 2D Coherence Factor performance, and more specifically, if it performs better on blockages in the elevation direction. In addition, it will look into some different types of image views used within echocardiography, and examine if certain views do better with the 2D Coherence Factor technique.

2 Theoretical Background

This chapter is intended to provide some general theory of the workings of ultrasound imaging technology. The purpose is to become familiar with the basics and also gain knowledge on some important underlying concepts relevant to this paper.

2.1 Principles of Ultrasound Imaging

Ultrasound waves are longitudinal acoustic waves used for a broad spectrum of applications. Ultrasound waves are not audible to humans, as the most common range of frequencies used in diagnostic ultrasound is from 1 to 20 MHz [17].

Ultrasound imaging is based on the phenomena of scattering. When ultrasound waves travel trough a medium and hit scatterers, some part of the ultrasound beam will be reflected. This reflected beam holds information on the location of the scatterer, and can be used to gain insight into the nature of the medium. These scatterers are spatial fluctuations in the mechanical properties of the medium, and in the case of diagnostic ultrasound this medium is body tissue. The mechanical property causing the reflections is called the acoustic impedance. The acoustic impedance is defined in equation 2.1.

$$Z = \rho c \tag{2.1}$$

where c is the speed of sound in the medium and ρ is the density of the medium [17].

2.2 Image Generation

The ultrasound beams are emitted from a device known as a transducer. The transducer can have a wide array of setups and geometries, but consists of some form of array of transducer elements. These elements are made up of piezoelectric materials, which have the property that they can vibrate at a certain frequency when coupled to a oscillating voltage source [18]. In this way the transducer can be used to transmit an acoustic signal. The same transducer can also be used on receive, as the piezoelectric elements can absorb acoustic waves and turn these into electrical signals.

The shape and size of the ultrasound probe will vary depending on application. The main types of probes are the linear array, the phased array and the curvilinear array. The linear array is large and flat and consists of bars. Not all elements are used simultaneously, only a subset. The linear array produces a square image. The phased array on the other hand is often called a cardiac probe and is smaller than the linear probe. The elements are narrower than for the linear probe. The phased array is explained in more detail in section 2.4 on echocardiography. The curvilinear array is physically curved and can image a wide area. It is therefore often used for fetal imaging.

The transducer will emit pulses from the elements in various directions. For every set of pulses there is produced one scanline, and steering can be done to get scanlines from different angles. The ultrasound image will in the end be made up of a set of these scanlines.

Focusing is an important technique that is used both on transmit and receive to improve image resolution. On transmit, a single focus point can be chosen. A set of delays can be applied to the pulses being emitted from the individual elements so that the pulses arrive at a given point at the same time. This will cause positive interference and the reflected signal will be very strong from this particular area. The focus is set to the most interesting part of what is being imaged. In echocardiography this is generally the centre of the heart. On receive one can perform dynamic receive focusing, also known as dynamic receive beamforming. This involves sweeping the focus from shallow to deep in order to achieve focusing at many depths. The pulses originating from the various depths are summed with delays so they interfere positively and create a strong signal.

Sampling is another important factor in the imaging process. When sampling the ultrasound signal we wish to sample finely enough to not miss any details. Nyquist sampling theorem says that to avoid aliasing one must sample at at least the double of the highest existing frequency component [19]. Aliasing is folding of the frequency spectrum of the signal, and distorts the signal. In ultrasound it is sometimes said that one wants to have a 50 % beam overlap at the focal point [20]. This in turn defines a minimum distance between adjacent beams on transmit, and therefore defines a minimum number of beams that have to be used when imaging. If the beams don't overlap enough, or at all, valuable information can be lost between the beams.

2.3   Resolution

Improving the resolution can in many ways be viewed as the most important goal in ultrasound imaging. High resolution imaging makes the diagnostic process both easier and more accurate. There are two main types of spatial resolution in ultrasound imaging; resolution in the depth/radial direction and resolution in the lateral direction.

The imaging system itself can be described through the point spread function or PSF. The PSF demonstrates how an infinitely small point is imaged by the system [19]. Imaging systems are not perfect and the point will most likely be smeared to some extent. The PSF therefore indicates the spatial resolution of the system, with the width of the PSF indicating the lateral resolution and the height indicating the axial resolution.

2.3.1   Radial resolution

The radial resolution is dependent on the length of the pulse. The radial resolution defines how well we can separate structures in the axial direction. The shorter the pulse used, the better the radial resolution. Ideally, the length of the pulse would be equal to the wavelength of the system. However, due to resonance of the piezoelectric element this is not possible. A good imaging system has a pulse length as close as possible to λ. Common pulse lengths are $1.5\lambda - 2\lambda$ [17]. A shorter pulse duration means that two received waves originating from two closely spaced scatterers will be easier to separate. This prevents the two scatterers from being perceived as the same structure.

The equation for the radial resolution is often given as in equation 2.2 [17].

$$res_{axial} = \frac{1}{2} * spatial\ pulse\ length \tag{2.2}$$

2.3.2   Lateral resolution

There are a number of conventions that define the lateral resolution. A common denominator for these rules is that the resolution in the lateral direction is proportional to the wavelength and the f-number. If we use the Rayleigh approach, the resolution can be expressed as follows [17].

$$res_{lat} = 1.2 \cdot f\# \cdot \lambda \tag{2.3}$$

The f-number describes the ratio between the width of the aperture and the depth of focus.

$$f\# = \frac{D}{F} \tag{2.4}$$

D is the width of the aperture and F is the distance from the centre of the transducer to the centre of focus.

In order to get as small (i.e good) resolution as possible, we want both the wavelength and the f-number to be as small as possible. A short wavelength implies a large frequency. Large frequencies are not a problem to obtain, but they do result in a trade off. Increasing the frequency means that the ultrasound wave will not penetrate as deep. The attenuation is higher for these waves. Therefore, there is a trade off between frequency and the depth of imaging. If the object to be imaged lies deeper within the body, a high frequency can not be used and one has to settle for a poorer resolution. As a rule of thumb, the deepest we can see is at a depth of 200λ [17].

The other option is to have a small f-number. The ideal f-number is 1. This implies that the width of the aperture is as wide as the focus is deep. The focus depth will depend on the object being imaged. If we are imaging the heart, the focus should lie approximately in the middle of the heart, to get as clear picture as possible. In order to make up for a deep focus, the aperture should also be wide. This is easy in some cases, like imaging of the carotid artery. In the case of echocardiography, a large probe is not practical. The bones of the rib cage provide too strong a reflection, so the probe needs to fit between the ribs. This means that the probe has to be small and in turn the maximum aperture width is smaller. This is another trade off that has to be made.

2.4   Echocardiography

There are a number of important sub fields within the field of medical ultrasound imaging. Echocardiography is ultrasound of the heart, and is a very important diagnostic tool for

cardiologists. Ultrasound is both a cost effective and non-invasive technology, and has therefore become an important tool for clinicians [21]. Echocardiography can be used to diagnose certain heart conditions like mitral stenosis or myocardial infarction and also monitor heart conditions, examine the hemodynamics and the functioning of the heart [22].

There are many different types of echocardiography, the most common one being thransthoracic echocardiography (TIE). TIE places the probe on the outside of the body pointed towards the heart. Other variations include Doppler echocardiograms, which are especially useful for examining the hemodynamics of the blood, as the Doppler ultrasound can pick up and visualize blood flow throughout the heart [22]. Transesophageal echocardiography (TEE) is another variation, albeit a more invasive one as it involves the insertion of a transducer through the esophagus using an endoscope. TEE can give clearer images where TIE fails to, as the heart rests close to the esophagus and the ultrasound beams have a short path to reach the heart [23].

The ultrasound method used to image the patients in this paper is the transthoracic method. This does involve some challenges, as the rib cage lies between the heart and the probe on the skin. There is a large difference in the impedance of the tissue surrounding the ribs, and the ribs themselves. This means that if the ultrasound beams were to hit the rib cage when travelling towards the heart, a high degree of the signal energy will be reflected. This means that the probe used for echocardiograms needs to be smaller than probes used for something like fetal imaging. A smaller probe size leads to a smaller aperture, and a smaller aperture yields a lower resolution for a given focus depth, as equation 2.3 indicates. The probe most commonly used is the cardiac probe, also called the phased array. Figure 2.1 shows the phased array (centre) beside a linear array on the left and a curvlinear array to the right. It is apparent from the figure that the phased array is substantially smaller than the other two arrays.

Figure 2.1: Linear array(left), phased array(centre) and curvlinear array(right)

The heart consists of four chambers, the two upper ones are the left and right atrium, and the two bottom chambers are the left and right ventricle. It is the contraction and relaxation of the different chambers that creates the heartbeat. The right side of the heart pumps deoxygenated blood to the lungs, and the left side of the heart receives blood from the lungs and pumps it to the rest of the body [24]. There are four valves in the heart; the aortic, mitral, tricuspid and pulmonary valve. These valves ensure the blood only flows in one direction [24]. A simplified view of the heart and its main anatomic components can be seen in figure 2.2.
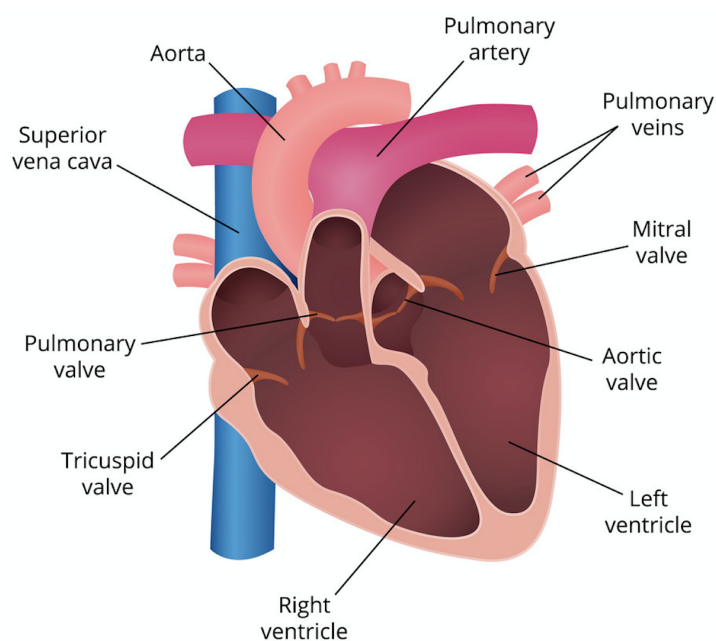
Figure 2.2: Basic heart anatomy. Picture borrowed from google.com

Heart ultrasounds are not as detailed as the above model, and depending on the cross section the imaging is performed with, the heart will appear different. Figure 2.3 shows a typical view of the heart during an ultrasound. Other imaging angles can lead to the heart appearing mirrored and upside down. The left and right ventricle and the left and right atrium are indicated in the figure. Imaging these valves, chambers and the borders between them clearly is important when performing an accurate clinical examination of the heart.
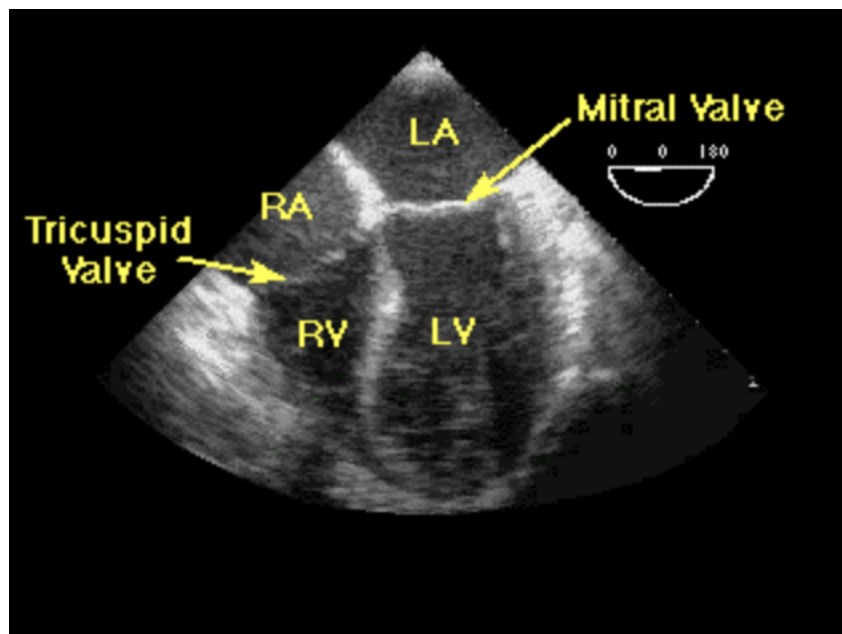
Figure 2.3: Still image from echocardiogram. Picture borrowed from google.com.

2.5   Ultrasound Image Signal Processing

Signal processing is a vital tool in in ultrasound imaging. The ultrasound RF signal can be altered in ways that improve the quality of the image. This section explains some of the most important signal processing techniques, and the techniques that were used in this thesis.

2.5.1   Harmonic filtering

Harmonic filtering, also known as harmonic imaging, is a technique where another frequency than the fundamental one is used for imaging purposes. The harmonics of an ultrasound signal build up as the pulse propagates through the tissue on transmit. The harmonics

can be created by the tissue itself, but also by contrast agents that can be injected into the tissue.

During transmit, a band of frequencies centered at the fundamental frequency is transmitted. At receive, this leads to a number of frequency bands. If the fundamental frequency is 2 Mhz, the harmonic bands will appear at multiples of this frequency, i.e at 4 Mhz, 6 MHz etc. [1]. Figure 2.4 shows the frequency content at 0 cm penetration (the dotted line) and then the frequency spectrum at 10 cm penetration (the solid line). At 0 cm there is no harmonic content, while at 10 cm depth the received signal has harmonic frequency components at up to 6 times the fundamental frequency.
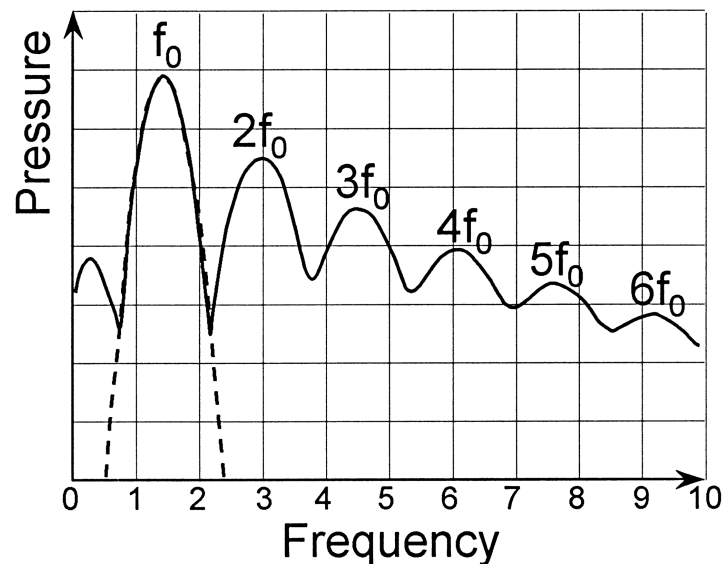
Figure 2.4: Fundamental frequency band and the harmonic bands. Reprinted from [1].

Harmonics build up due to the non-linearity of the acoustic medium. The nonlinear tissue causes the peaks of the pulse to travel faster than the troughs, causing a skewed pulse resembling a saw-tooth pulse. While the fundamental frequency is attenuated linearly with depth, the harmonics increase with depth until tissue attenuation counteracts this phenomenon and causes the harmonics to decrease [1]. The distortion at 0 cm (dotted line) and 10 cm (solid line) is illustrated in figure 2.5.
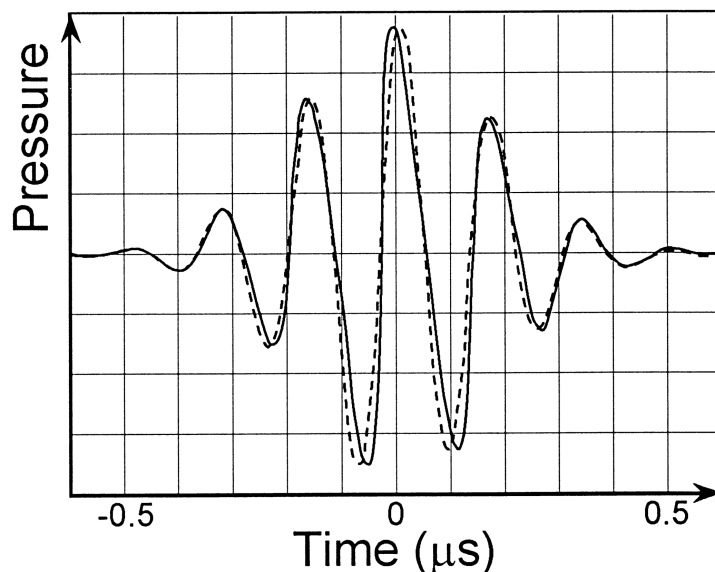
Figure 2.5: Distortion of ultrasound pulse. Pulse shape at 0 cm(dotted line) and pulse shape at 10 cm(solid line). Reprinted from [1].

In ultrasound technology, it is the second harmonic that is most commonly used for imaging. This is primarily because higher harmonics give too little signal energy to form images, as they are attenuated too much [25]. One of the main advantages of harmonic imaging lies in the reduction of clutter and noise. The phenomenons that lead to scattering and distortion, e.g reverberation artefacts and sidelobes, have a much lower signal energy than the transmitted signal [1]. Therefore, they do not contribute significantly to the generation of harmonics. Also, due to the fact that the harmonic beams are mainly generated at the centre of the ultrasound beam, the width of the beam is narrowed leading to an increase in lateral resolution [25]. In addition, the signal-to-noise ratio (SNR) is increased, and the resolution at deeper depths is frequently improved [1].

2.5.2   Beamforming

Beamforming is an essential signal processing tool in ultrasound. Its primary use is to create interference patterns of the received beams in order to improve focusing and other characteristics of the image. The most common type of beamforming is known as delay-and-sum beamforming, shortened DAS. As the name indicates, the beams returning to the various channels are delayed so that they arrive in-phase. The reflections from a scatterer have to travel different distances to reach the various elements of the transducer. This means they arrive with a phase shift relative to each other. The sum indicates that

after delays are applied the signals are added together.

The concept is illustrated in figure 2.6. The image shows the reflected waves from the scatterer in red, arriving at the probe. The column of blue wave pulses are not arriving coherently at the probe. After the time delays are added, the signals arrive coherently, and, after apodization, the signals are summed into what is known as the RF signal. Apodization is a tool often used for sidelobe suppression, and involves a modification of the aperture, often by something called an apodization mask. This mask can be a window function, like the Hamming window.
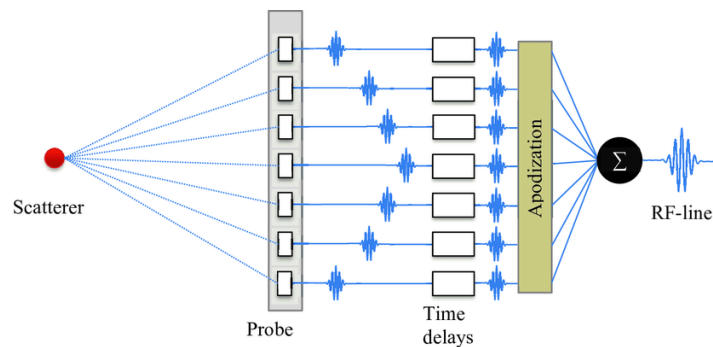
Figure 2.6: DAS beamforming. Reprinted from [2].

2.5.3   Scan conversion

For echocardiographic purposes, the phased array is the preferred array. When imaging, the phased array sends out the radial scan line in a sector shape, with every beam at a given angle from the transducer surface. However, when sampling the received signals, the resulting data is collected and stored in an array, and the geometric nature of the ultrasound data is lost.

In order for the ultrasound images to have a layout that is biologically correct, the coordinates of the data must be transformed to take into account the nature of the received data. The layout of the imaged object will not make sense if not. Scan conversion is the process of converting the ultrasound data from polar coordinates into Cartesian coordinates [26].

2.6 Coherence Factor Imaging

Coherence factor imaging is an adaptive technique that exploits the varying degree of coherence across the image to suppress unwanted artifacts, like sidelobes. Coherence in an ultrasound context is the degree of how coherently, or in phase, signals arrive at the transducer surface. The technique calculates the ratio of coherency to incoherency in the image, and then uses this ratio to weight the image. There are a number of ways of calculating the coherence, and a wide array of ways to use coherence to improve ultrasound images. The two most relevant to this paper are the Coherence Factor presented by Mallart and Fink [11] in 1994, and the 2D Coherence Factor presented by Fatemi et al. [3] that this paper is examining.

2.6.1 The Coherence Factor

One way of calculating the Coherence Factor was outlined by Mallart and Fink in 1994 [11]. The Coherence Factor, introduced as the Focusing Criterion, is found by calculating the ratio of coherent energy over the transducer array to the incoherent energy. This is summarized in equation 2.5.

$$CF(z, \phi) = \frac{|\sum_{m=1}^{M} \sum_{n=1}^{N} s_{mn}|^2}{MN \sum_{m=1}^{M} \sum_{n=1}^{N} |s_{mn}|^2} \tag{2.5}$$

The array is modelled as a MxN array where M is the number of elements in the azimuth direction, N is the number of elements in the elevation direction and s_{mn} is the signal value received by element (m, n) from depth z and at beam angle ϕ. This is a simplified notation to make the formulas cleaner, and the signal is expressed as in equation 2.6. s is the signal arriving at element (x,y) on the coordinate system, from depth z and beam with angle ϕ

$$s_{mn}(z, \phi) = s(x, y, z, \phi). \tag{2.6}$$

The received signal for given angle ϕ originates from point (x, z) in the imaging plane, as the ultrasound beam is transmitted at $y = 0$. This is illustrated in figure 2.7.
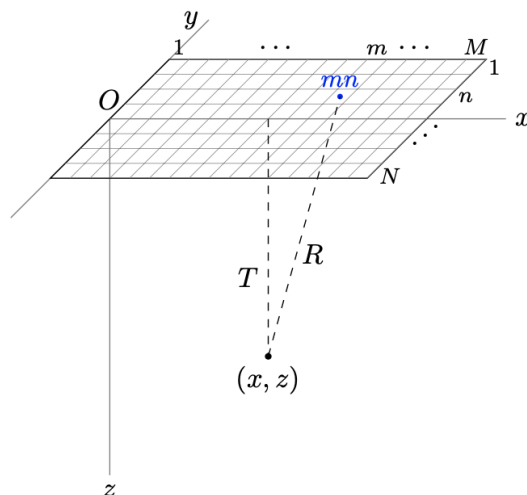
Figure 2.7: Geometric representation of the MxN transducer array. Reprinted from [3]

The nominator of the sum in equation 2.5 is the coherent intensity. This sum is coherent because it sums the signals before taking the absolute value, therefore taking into account signals summing in coherence. The denominator is the incoherent intensity, and it is the incoherent intensity received by one element, in this case (m,n), multiplied by the total amount of elements, MxN. The absolute value is taken before the sum is calculated, removing the possibility of signals summing in phase.

2.6.2   The 2D Coherence Factor

The 2D Coherence Factor is one of many ways to exploit coherence in the quest to improve image resolution. It is based on the coherence calculations by Mallart and Fink, but adapts the formula to account for local spatial variations of the coherence.

The method is presented in the paper titled *Row-based coherence imaging using a 2D array transducer* by Fatemi et al. The novelty lies in the exploitation of the spatial variations in coherence across the transducer array. The degree of coherence is often non-uniform across the array, as structures like the ribs can sometimes only partially block the ultrasound beam. This means that we get incoherent reverberations on only some part of the probe. Fatemi et al. [4] have written a separate paper on the effect this has on the transducer. In this paper it is demonstrated through a number of experiments how, in many situations, only some of the ultrasound beams hit a lung cavity or a rib. Fatemi et al. claim that this in all likelihood means that the reverberations and reflections created by a lung or

a rib will be received by only a part of the transducer. Examples of this can be seen in figure 2.8. The left illustrations shows that only part of the lung (coloured red) is blocking only part of the ultrasound beam. The illustration on the right shows the same thing, however in the azimuth direction. The beams coloured red are the ones affected by the lung blockage.
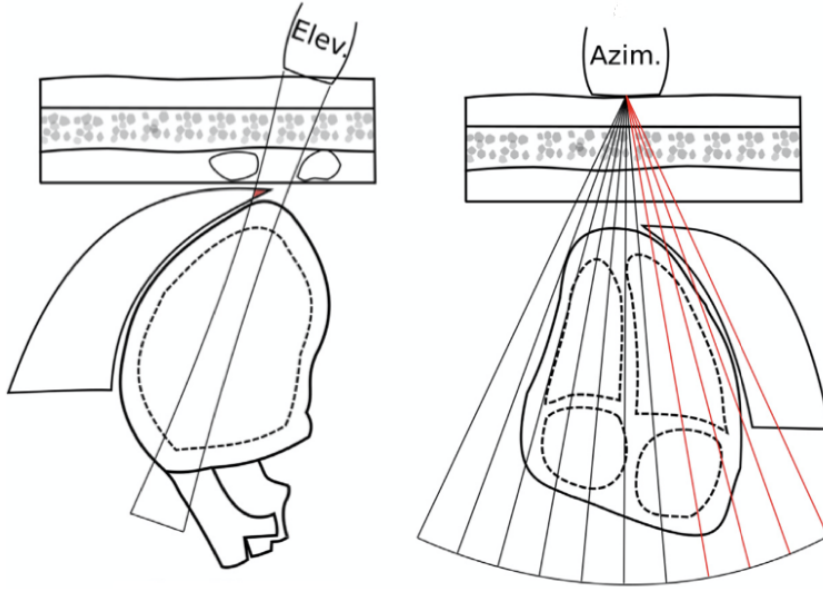
Figure 2.8: Illustrations showing the lung blocking a part of the ultrasound beam in the elevation direction (left) and the azimuth direction (right). Image adapted from [4].

The idea behind the technique presented in [3] is to exploit this to get even better clutter reduction.

The equation for calculating the 2D Coherence Factor looks much like the equation for the original Coherence Factor. In fact, if we set K=1 and N=K, equation 2.7 reduces to equation 2.5.

$$CF_{2D}(z,\phi) = \frac{1}{N-(K-1)} \sum_{k=1}^{N-(K-1)} \frac{|\sum_{n=k}^{k+(K-1)} \sum_{m=1}^{M} s_{mn}|^2}{KM \sum_{n=k}^{k+(K-1)} \sum_{m=1}^{M} |s_{mn}|^2} \qquad (2.7)$$

The graphic representation is similar to that of the Coherence Factor. The array is illustrated in figure 2.7. However, a new parameter K is introduced. K is the number of neighbouring rows being used for the coherence calculations, and is therefore the size of the moving window.

An illustration of the geometry of the transducer with the sliding window is seen in figure 2.9. Here the size of the sliding widow is set to $K = 3$ and indicated with the elements coloured red. This window will then move down the y-axis until calculations have been performed on all of the rows.

The choice of the parameter K is not arbitrary. In fact, when deciding on the value of K there is a trade-off between resolution in the elevation direction and the degree of clutter suppression [3]. An experiment was done by the authors of paper [3] to determine the optimal value of K. It was found that a K value of 5 gave a resolution in the elevation direction that was comparable to that of DAS imaging.
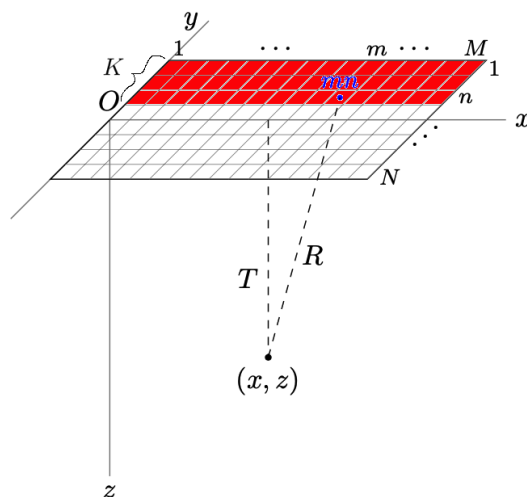
Figure 2.9: Transducer geometry with the sliding window of K rows

Fatemi et al. hypothesize that the reverberations that lead to clutter only hit part of the aperture, and that by dividing the aperture into smaller subsets one can suppress the contribution from the subsets with low coherence. The elevation direction is chosen for the 2D CF, which could imply that the algorithm should work best at improving images that have blockages in the elevation direction.

2.6.3   Application of the coherence factor

As indicated in the two previous subsections, there are a number of ways the coherence factors can be calculated, and two have been presented in this paper. However, the application of this coherence ratio to the imaging process is similar for both the Coherence Factor and the 2D Coherence Factor. They are used as an adaptive weighting grid for the

DAS image. This was initially done by Li and Li in [12]. The coherence grid is made up of values between 0 and 1. Values close to 0 exhibit incoherence, while values close to 1 exhibit high coherence. When this grid is multiplied with the DAS image, the areas of low coherence (e.g sidelobes) will be multiplied with small values, and thereby suppressed. Values with high coherence will be multiplied with values close to one, and therefore kept nearly as is.

The weighting can be expressed through the relation in equation 2.8 where I is the DAS image, C the coherence factor and I_c the coherence weighted image.

$$I_c = I \cdot C \tag{2.8}$$

3 Method

The aim of this paper was to study whether the 2D Coherence Factor improves the image quality, and if the nature of the aperture energy blockages have any connection to how well the processing tool works. This was performed by processing the data and then analyzing it in three steps. The processing of the ultrasound images was done in MATLAB (The MathWorks inc, Natick, USA) using a toolbox called USTB. The data from the 9 patients was processed using MATLAB code and the resulting images were combined into videos and further analyzed.

3.1 The Data

The data used in this thesis is ultrasound data taken from 9 patients at St. Olavs Hospital in Trondheim. Two cardiologists are behind the collection of the data, and the collection is approved by the *Regional Committee for Medical and Health Research Ethics (REK)*. The patients were being evaluated for heart disease, specifically valvular disease. The data was collected using an E95 (GE Vingmed Ultrasound AS, Horten, Norway) ultrasound scanner and a 4Vc-D 2D array probe. The ultrasound scanner was set up with the default cardiac application, which involves second harmonic imaging at a frequency of 3.4 MHz.

For every patient, the heart was imaged using 5 different cross sections or image views. Different image views are obtained by moving the probe and holding it in different positions and angles. The views used during image acquisition are presented in table 3.1

Cross section	Full name
PLAX	Parasternal long axis
PSAX	Parasternal short axis
A4C	Apical four chamber
A2C	Apical two chamber
ALAX	Apical long axis

Table 3.1: Cross sectional views and their explanations.

For every image view, 64 ultrasound images were taken. This means that for every patient, there is 5x64 ultrasound images to process.

3.2   USTB

The UltraSound ToolBox(USTB) is a MATLAB toolbox used for processing ultrasound images. It is the result of a joint effort between a number of ultrasound research environments, UiO in Oslo and NTNU in Trondheim among other places. The idea behind the toolbox is to be able to compare ultrasound images in a more accurate way [27]. The toolbox defines both a file format, $.uff$, and a framework to create a pipeline for image processing that is compatible with all kinds of transmit sequences [27]. Figure 3.1 illustrates the layout of both the toolbox and the UFF file format.

The pipeline lets the user implement various stages of the beamforming process through three steps defined as either a preprocess, a midprocess or a postprocess. The preprocess is often a form of complex demodulation, a technique used to move the frequency content of the signal to baseband in order to reduce the sampling frequency among other things. The midprocess takes the output from the preprocess as input and is the delay-and sum beamformer. Delays are applied to the channel data, and depending on further processing they are either summed or not. The output of a midprocess is passed on to the postprocesses. Examples of postprocesses are different types of beamforming and coherence factor calculations, for instance the GCF and the DMAS beamformer.
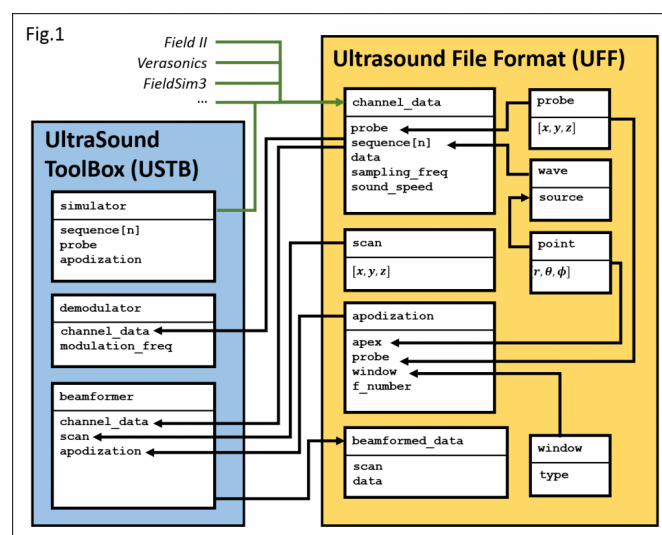
Figure 3.1: The USTB file format and UFF class. Reprinted from [5].

3.3   Image Processing

In order to explain the method of how the images were processed in an organized manner, the procedure has been split into a number of components. These are the most important steps in the implementation of the image test code.

3.3.1   Harmonic filtering

Harmonic filtering was performed to extract the second harmonic from the harmonic data. In order to pick out and isolate the second harmonic, the power spectrum of the data can be plotted, as has been done in figure 3.2. The data was filtered with in MATLAB to remove the unwanted frequency components. The frequency content in the figure has been translated to the 0 frequency, i.e moved to baseband. The red graph is the signal after filtering, and it is apparent that the second harmonic data is isolated and the fundamental frequency is removed from the spectrum.
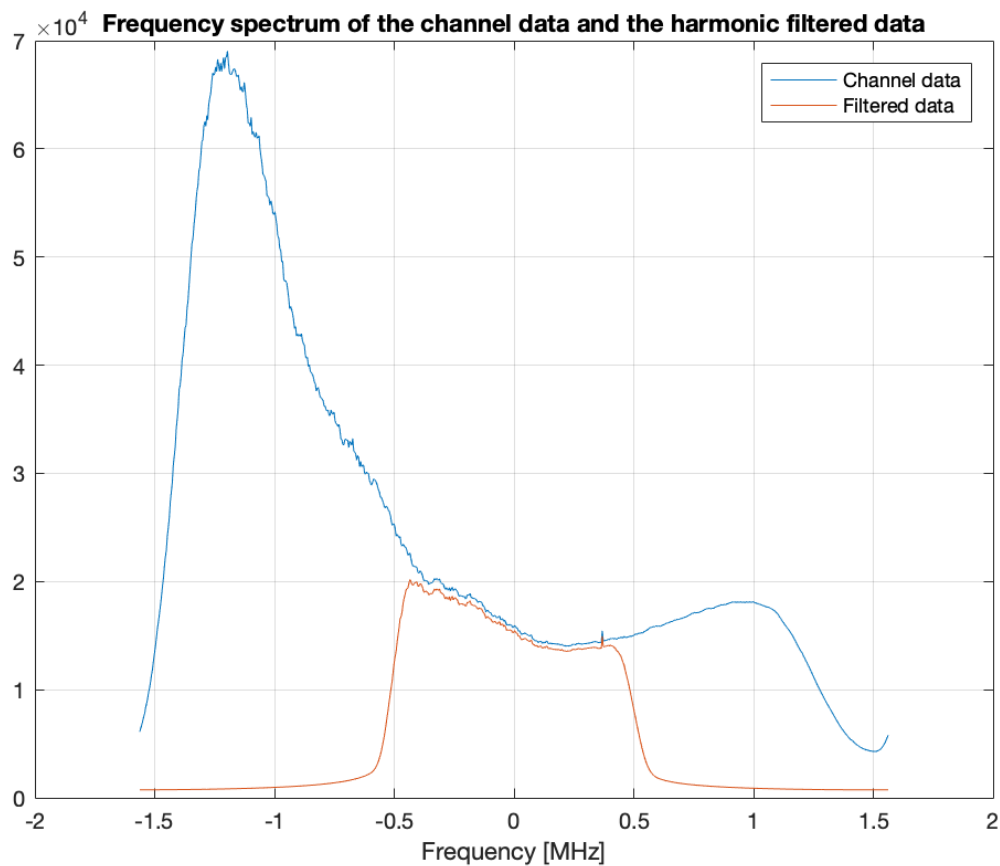
Figure 3.2: Plot of the frequency content of the channel data and the harmonically filtered data.

Figure 3.2 is specific to one patient, but gives and idea of how the spectral data was separated. The same filter was used for all patient data.

3.3.2   The scan setup

The scan setup was determined early on in the code, and set fundamental properties like the imaging axes and scan depth. The depth axis was set to a linearly spaced axis with 256 points. The values range from 0 to the depth of the ultrasound acquisition. The azimuth axis was defined using the properties of the USTB channel data object.

The final step of the scan setup was declaring the scan type, which was a sector scan. The axes of the sector scan are as defined above.

3.3.3   The pipeline

The image processing was carried out in MATLAB. Using USTB, a pipeline including a delay and sum midprocess was combined with different postprocess' depending on the sought technique.

The DAS midprocess used a hamming window apodization function for both transmit and receive, and the parameters can be found in table 3.2.

Parameter	Transmit	Receive
Window	Hamming	Hamming
F number	5	1.5

Table 3.2: Apodization types and parameters.

A coherence factor postprocess generated the Coherence Factor, and the two dimensional coherence factor postprocess generates the 2D Coherence Factor.

3.3.3.1   Coherence Factor postprocess

The postprocess code for the Coherence Factor presented by Mallart and Fink [11] is implemented as a process in the USTB library. The postprocess is performed on the object returned by the midprocess explained above. The Coherence Factor is calculated using equation 2.5. The receive apodization was set to the same as in table 3.2, and the process returns both the Coherence Factor itself, and the weighted coherence image .

3.3.3.2   2D Coherence Factor postprocess

The postprocess for the 2D Coherence Factor is quite similar to that of the simple coherence factor postprocess. However, the algorithm is based on equation 2.7. The transmit and receive apodization was set to the same as in table 3.2. The size of the sliding window was set to $K = 5$ because, as discussed in Chapter 2, this is the choice that gives the best results according to [3]. As with the Coherence Factor postprocess, both the 2D Coherence Factor and the weighted image were returned for further processing.

3.3.4   Histogram matching

When using visual comparison as a tool in research, it is of the utmost importance that the images are displayed in a way that makes them visually comparable in a correct manner. Images can be manipulated to look a multitude of different ways. To make sure the ultrasound images could be accurately compared, a technique called histogram matching was employed. The histogram of the DAS image was used as a reference, and the histograms of the CF and 2D CF were matched to the reference histogram.

The reference image was created using the scan converted DAS image, I_{DAS}. This image is then scaled using the minimum and maximum value of the DAS data, D_{min} and D_{max}. The equation for the scaling is shown in equation 3.1

$$I_{scaled} = \frac{I_{DAS} - D_{min}}{D_{max} - D_{min}} \tag{3.1}$$

The data for the scan converted CF data and 2D CF data were scaled in the same manner as the DAS data, using the approach from equation 3.1 and the min and max from the CF and 2D CF data. The histograms were then matched using a MATLAB histogram matching function called *imhistmatch*. The number of bins was set to 1024 in both cases. After the images were matched, they were converted back into dB scale by use of the formula in equation 3.2 and the min and max of the reference image.

$$I_{dB} = I_{scaled} \cdot (I_{scaled} - D_{min}) + I_{scaled} \tag{3.2}$$

By matching the histograms, the intensity levels of the two images are ideally equivalent,

and they are possible to accurately compare. This is done by minimizing the error in intensity between the histogram of the reference image and the histogram of the image to be matched [28].

3.3.5   Data visualisation

In order to visualize a possible improvement, four videos were created for every image view presented in table 3.1. This means that 20 videos were generated per patient. Table 3.3 summarises these videos and what their purpose is.

Video name	What it shows
CF vs CF 2D	Compares the weighted images of the two coherence factors to each other.
DAS vs CF 2D	Compares the DAS images to the weighted 2D CF image.
DAS vs CF	Compares the DAS images to the weighted CF image
CF grid vs CF 2D grid	Compares the CF grid to the CF 2D grid.

Table 3.3:   Overview of video types.

The videos were generated using a MATLAB tool called *videoWriter*, which uses the processed ultrasound image to create a sequence of figures. The images were created using a function called *imagesc*, with the colormap set to grayscale for videos 1-3 and to default for video 4. The default colormap for MATLAB is a PARULA color map.

For every frame, a figure was created. The figure was a subplot of the two images to be compared, e.g for the first video, the subplots were of the CF weighted image and the 2D CF weighted image. Image 3.3 shows such a figure.
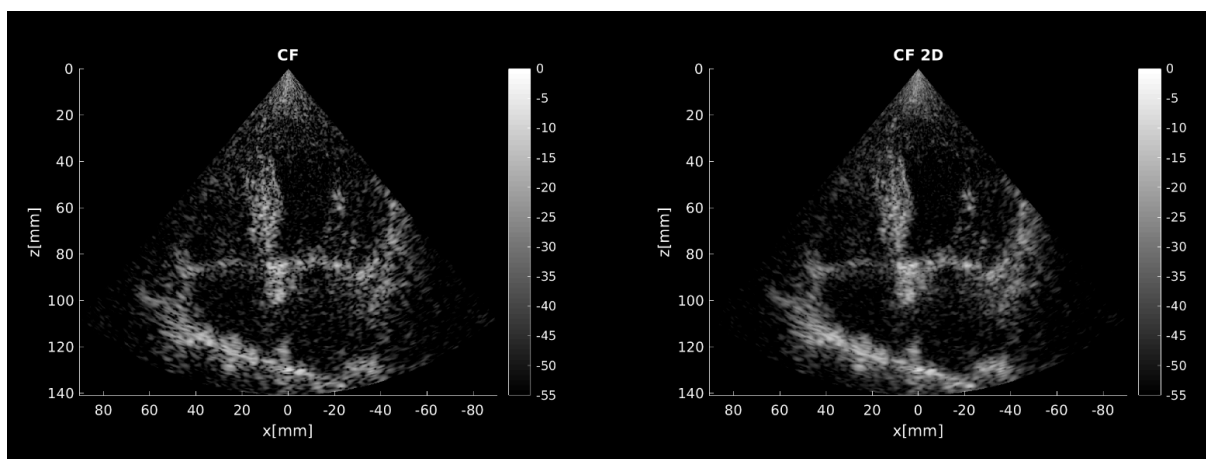
Figure 3.3:   Example of a subplot that is basis for a video.

When all 64 figures were created, they were combined into a video using *videoWriter*. The frame rate was set to 25, which means that the videos show 25 frames per second.

3.3.6   Aperture energy plots

The algorithm under scrutiny relies on the assumption that the aperture is blocked in a certain way. In order to investigate these claims the energy over the aperture was plotted. The aperture energy was plotted for every beam and displayed in a mesh grid. The channel data is denoted as $y(i, j, k, l)$, where i is the number of range samples, j the number of elements, k the number of beams and l is the number of frames. The amplitude information of the channel data is found by using a specific range of elements. The range start, R_s was chosen to be $0.3 * N_{samples}$ and the range end, R_e was set to the total number of samples, $N_{samples}$. The aperture energy was calculated for the last 70% of the samples to avoid the expanding aperture that is applied in the near field. The channel data is complex, and the absolute value was taken to remove the phase information but keep the amplitude information. The mean over the range of samples was then taken, as expressed in equation 3.3. $P(j, k, l)$ is the channel data after the mean over the range samples is taken.

$$P(j, k, l) = \frac{1}{R_e - R_s} \sum_{i=R_s}^{R_e} \mid y(i, j, k, l) \mid \tag{3.3}$$

The mean was also taken over the fourth dimension l, the frames. This was done because it is assumed that the probe is kept still during the data acquisition. This resulted in $P(j, k)$. The energy over the aperture, $A(j, k)$ was found by squaring $P(j, k)$. The maps were displayed in decibel scale, so the logarithm was taken. This is summarized in equation 3.4

$$A(j, k) = 20 * \log_{10}(P(j, k)) \tag{3.4}$$

Two different amplitude plots were generated, one normalized with respect to the maximum across all beams, the other normalized with respect to the individual maximum value of each beam. The normalization of the former case is done using the simple formula in equation 3.5. The max-operator returns a single number in the case below.

$$A(j,k) = A(j,k) - \max_{\{j,k\}}\{A(j,k)\} \tag{3.5}$$

The normalization of the latter aperture map is performed for each beam individually, by using equation 3.6. The max operator in this equation returns one value for every beam.

$$A(j,k) = A(j,k) - \max_{\{k\}}\{A(j,k)\} \tag{3.6}$$

An example of the former is given in figure 3.4, while the later is given in figure 3.5. The second plot is more relevant to this thesis. The bar to the right of the plot indicates the decibel value of the received signal energy. The plot is organised with beams 1 to 113 following the rows. The example in figure 3.5 shows that the energy over the aperture is high and quite uniform for the first and last beams. In the middle however, the energy is not uniform and there are areas where the energy is dipping as lows as 30 dB below the maximum energy value. This is a large variation in received signal energy across the aperture, and could indicate a blockage of some kind. The nature of the blockage in this case is variant mostly in the azimuth direction.
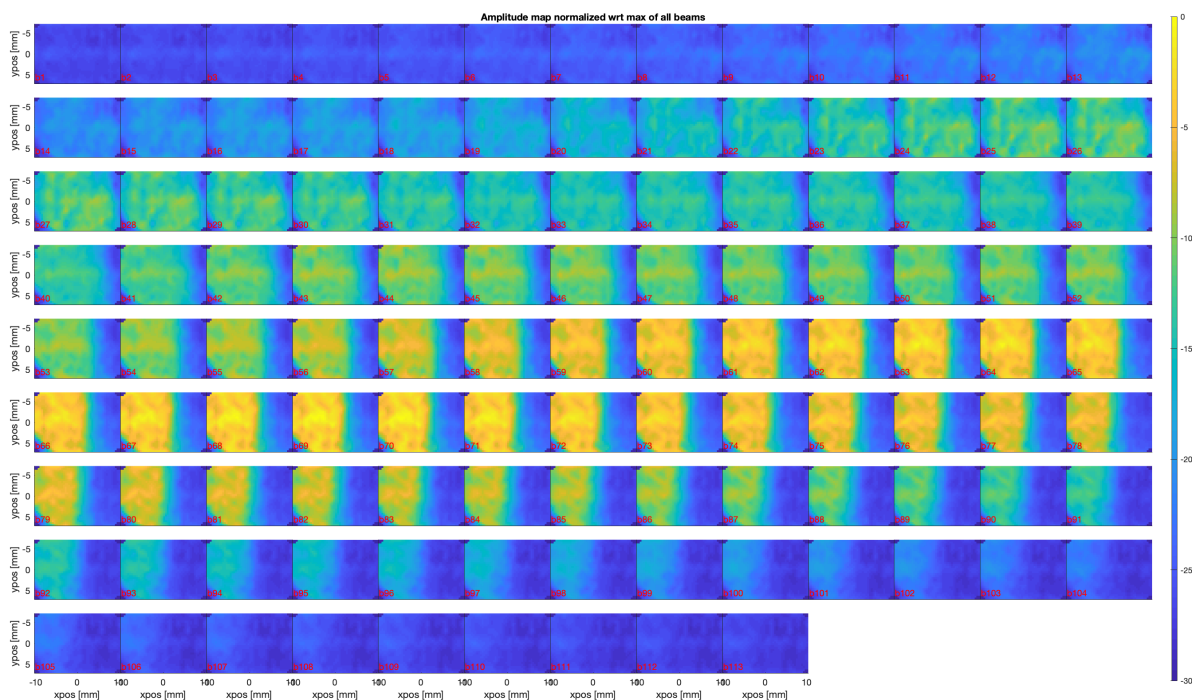
Figure 3.4: Aperture energy map normalized using the max across all beams.
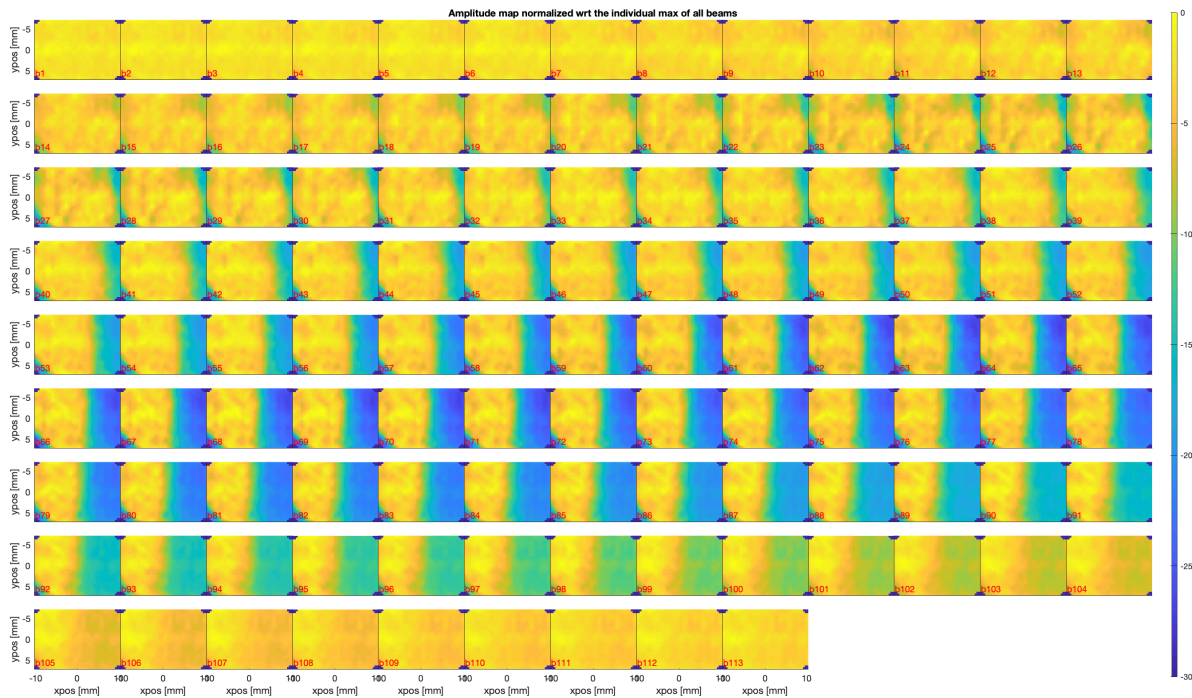
Figure 3.5: Aperture energy map normalized using the max of every beam individually.

Another way of visualizing the potential blockages of the aperture is to calculate the number of elements with a decibel value below a certain threshold. Trials were performed to determine the most accurate threshold value, and -12 dB turned out to be the most fitting. By calculating the percentage of elements with amplitude lower than this threshold value, the following graphs were created.
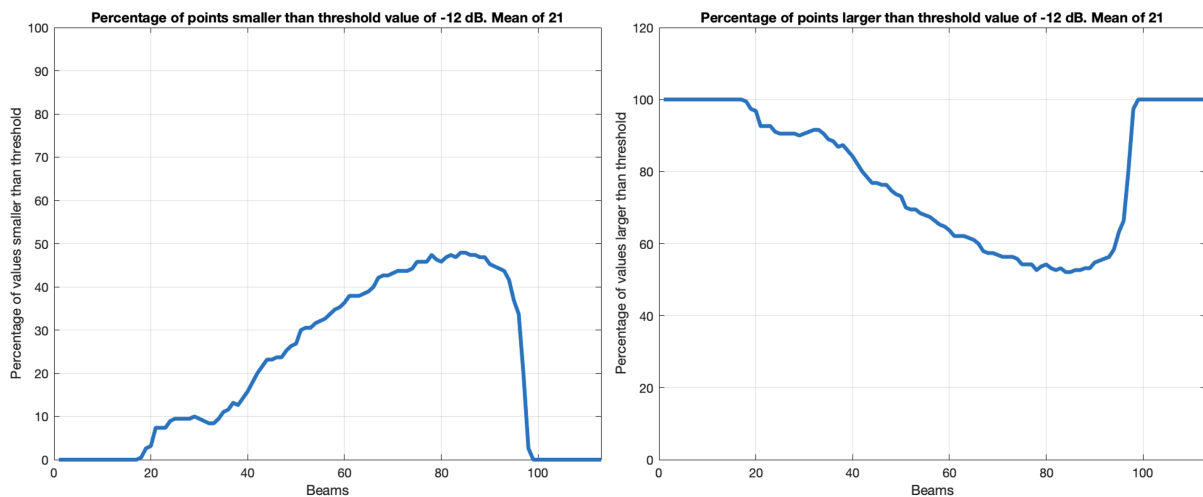
Figure 3.6: Percentage of values lower than threshold (left) and percentage of values higher than threshold (right).

Figure 3.6 shows two plots. The left plot indicates the percentage elements lower than the

threshold for each beam. The right plot is an alternative way of visualizing the same data. It shows the percentage of elements with values higher than the threshold per beam. The plots show that there are blockages as high as 50% for beams 80-90. By comparing this to the aperture energy map in figure 3.5 we can verify that the blockage of signal energy grows and is largest for beams number 80-90.

The percentage of blocked elements for all beams was also calculated. The mean percentage value M for the plots is indicated in the title of the plots in figure 3.6. In this instance the mean percentage is 21% blocked elements across the whole aperture for all beams. Equation 3.7 explains how this is done. The function $p(beams)$ is the percentage of blocked elements for beam number $beams$. N_{beams} is the total number of beams.

$$M = \frac{1}{N_{beams}} \sum_{beams=1}^{N_{beams}} p(beams) \tag{3.7}$$

3.4   Data Analysis

The data was analyzed in three steps with a slightly different approach and focus for each stage. The first step studied the data and focused on the quality of the different videos. The second step concentrated on examining how the aperture energy plots of the videos differed. Lastly, the third step was to group the videos by which image view they were taken with, and the image quality of these groups was examined.

3.4.1   Preliminary examination of image quality

The initial step in the analysis of the data was to start examining the data systematically. The videos were watched one patient and one cross section at a time. For every video, a small comment on the differences in image quality was noted in an Excel document. A section of this document and how the observations were structured can be seen in the screenshot in figure 3.7. The columns *patient* through *CF grids* were filled out. All the videos were watched as it was not initially decided that only the CF 2D and the DAS were to be compared.

Patient	Cross section	CF vs CF 2D	DAS vs CF 2D	DAS vs CF	CF grids
	PLAX	CF 2D has subtly better borders.	Structures have better visibility for th	Cleaner DAS but CF picking up some structures DAS is not.	CF 2D more accurate.
	PSAX	Quite noisy. CF 2D performs best.	Quite similar, slightly less cavity noise for CF 2D.	Difficult to say. DAS best?	CF 2D best.
	A4C	Both good and difficult to separate.	CF 2D clearer.	DAS possibly better due to cavity walls.	CF 2D best.
	A2C	CF 2D a bit better	Nearly identical.	DAS less noisy.	CF 2D slightly better.
67	ALAX	CF 2D picking out structures better.	CF 2D crisper.	Not easy due to CF noise.	CF 2D i think?
	PLAX	Clearer for CF 2D	CF 2D shows improvement on borders.	Possibly clearer borders for CF, but very corrupted by noise compared to DAS.	Unclear. Better 2D.
	PSAX	Difficult to see difference. Better intensity level for CF but less noise in cavity for 2D.	2D better than DAS.	More noisy CF but better intensity.	Better 2D.
	A4C	Better borders for CF. Also less noise in cavities.	Crisper imaging for 2D.	Possibly clearer borders for CF, but corrupted by noise compared to DAS.	Better 2D.
	A2C	CF looks crisper than 2D.	Small improvement for 2D.	CF better than DAS.	Difficult to pinpoint difference. CF slightly better?
68	ALAX	CF 2D better borders and less noise.	Better 2D.	Clearer but more speckled CF.	better 2D.

Figure 3.7: Example of spreadsheet document used for the first look at videos.

The colour indexing in the *cross section* column was applied to indicate which videos initially appeared to have better CF 2D over DAS performance (green) and poorer CF 2D performance (red). The videos that show a slightly better performance, no improvement or where it was hard to tell the difference, were marked in yellow. An example of a video that could be placed in the yellow category is a video where some frames show an improvement with the 2D CF and some frames show little to no difference. The colour codes are summarized in table 3.4

Colour	Meaning
Green	The 2D CF image shows a clear improvement compared to the DAS image.
Yellow	The 2D CF image shows little to no improvement compared to the DAS image
Red	The 2D CF image has reduced quality compared to the DAS image.

Table 3.4: Explanation of the colour codes.

The videos were then grouped into these colour categories and studied further.

3.4.2   Examination of data from aperture energy maps

After the first step had been performed, every video had been examined and commented on. The videos had also been grouped into colour categories as explained in the former section. It was now time to consider the aperture energy data.

The aperture maps were initially studied for all the patients and all views. The geometry of the aperture map blockages was noted in a spreadsheet. An example from this spreadsheet can be found in figure 3.8. The mean percentage of blocked elements for the video was also noted.

Next, the colour categories were considered. A number of metrics were calculated for each colour category individually. These included distribution of blockage types and mean percentage of blocked elements. This made it possible to compare the colour category groups to each other.

Patient	Cross section	Type of blockage	Cross section name	Mean value	Blockage letter
	1	Some, both in top right corner and left side. Variant in both azimuth and elevation.	PLAX	0%	A E
	2	Top right corner. Both azimuth and elevation.	PSAX	0%	A E
	3	Top right corner, turning into top. Both directions, mostly azimuth.	A4C	0%	A E
	4	Slightly top right but mostly bottom left. Quite strong. Both azimuth and elevation	A2C	5%	A E
67	5	Left side so mostly variation in azimuth. Also some in elevation.	ALAX	2%	A
	1	Mostly left side, so variation in azimuth.	PLAX	0%	A
	2	Mostly top, so variation in elevation.	PSAX	0%	E
	3	Bottom, right hand and left hand corner. A lot of variation for elevation and azimuth.	A4C	0%	A E
	4	Bottom right, quite strong. Elevation and azimuth.	A2C	2%	A E
68	5	Top right hand, variation in azimuth and elevation both.	ALAX	1%	A E

Figure 3.8: Example of spreadsheet document used for examining the aperture maps.

3.4.3   Examination of data from image views

The third and last step of the data analysis was to categorize the data according to type of cross section, or view. The different types of image views are explained in section 3.1 of this thesis. The data collected in the previous steps was organized into 5 different categories according to the image views, each containing videos from the 9 different patients.

For every view group, data was collected on the mean percentage of blocked elements,

image quality category as well as aperture blockage types within the group. This was summarised for all the views individually, as can be seen in an example of the spreadsheet in figure 3.9.

PLAX						PSAX				
Patient	Aperture map	Mean value	Quality	Ap.letter		Patient	Aperture map	Mean value	Quality	Ap. Letter
67	Some, both in top right corner and left side. Variant in both azimuth and elevation.	0%		AE		67	Top right corner. Both azimuth and elevation.	0%		A E
68	Mostly left side, so variation in azimuth.	0%		A		68	Mostly top, so variation in elevation.	0%		E
70	Upper panel, mainly elevation direction.	0%		E		70	Upper right hand corner and top panel. Mainly elevation.	$		E
73	Little blockage. Slighlty in upper right hand corner. Both elevation and azimuth.	0%		A E		73	Right side and slightly corners. Both azimuth and elevation.	0%		A E
74	Upper right hand corner slightly blocked. Dot in centre.	1%		A E		74	Significant in bottom left corner. Dot in centre.	5%		A E
75	Upper right corner and dot. Azimuth and elevation.	4%		A E		75	Blockage in upperright corner and right side. Mostly azimuth but also elevation. Dot in centre	1%		A E
76	Slight blockage in upper panel. Dot. Elevation mainly.	1%		E		76	Mainly in upper right corner. Dot. Bot azimuth and elevation.	1%		A E
77	Upper right corner to upper panel. Mostly elevation.	0%		E		77	Top right and bottom right corner. Both azimuth and elevation.	0%		A E
80	No clear pattern.	0%		A E		80	Top right corner. Both azimuth and elevation.	0%		A E
Mean(%)		0,00666667				Mean(%)		0,00875		
Green		10	Yellow	0		Green		7	Yellow	2

Figure 3.9: Example of spreadsheet document used for examining the image views.

The spreadsheet shows the data of interest for the PLAX and PSAX views.

4 Results

Given that the examination of the data was performed in three separate parts, it is natural to present the results in the same manner. The results for the preliminary examination will be presented first, followed by results from the two other stages.

4.1 Preliminary Examination of Image Quality

As mentioned in section 3.4.1, colour codes were assigned to the videos. This colour coding was based on the videos comparing the DAS to the 2D Coherence Factor. Of these videos there were 45. The videos were studied frame by frame and also as a whole. The most important image quality parameters that were checked were the clarity of the borders, the noise and in general how clear the cardiac structures were.

4.1.1 Green category - videos that indicate an improvement

The videos that showed an improvement for the 2D Coherence Factor over the DAS have in common that the 2D Coherence Factor method improved the image quality in some shape or form. A few examples will be presented.
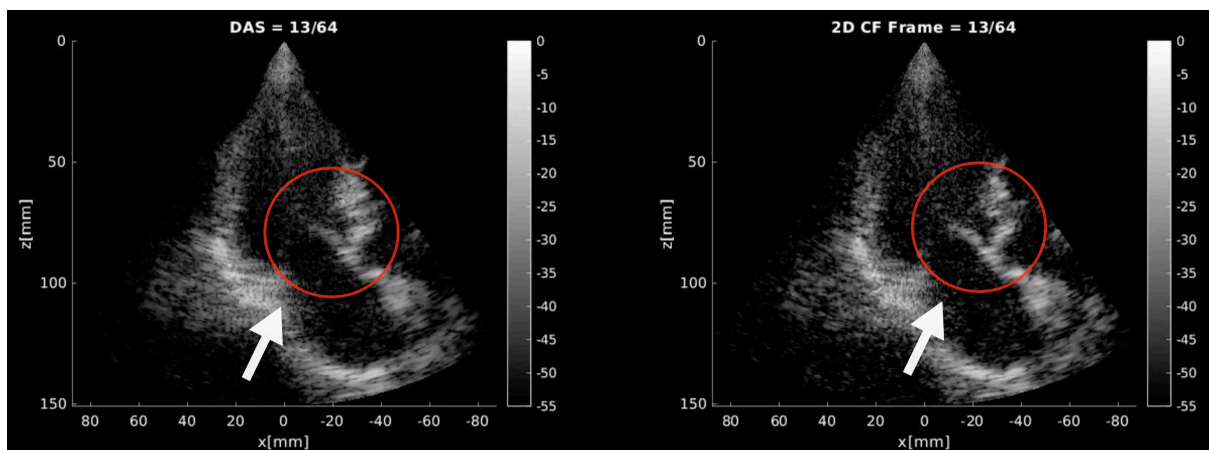
Figure 4.1: Ultrasound frame that indicates an improvement in 2D CF (right) over DAS (left).

Figure 4.1 illustrates the type of traits that would typically place a video in the green category. The circled structure is a lot more crisp and clear in the 2D CF frame (right) than the DAS frame (left).
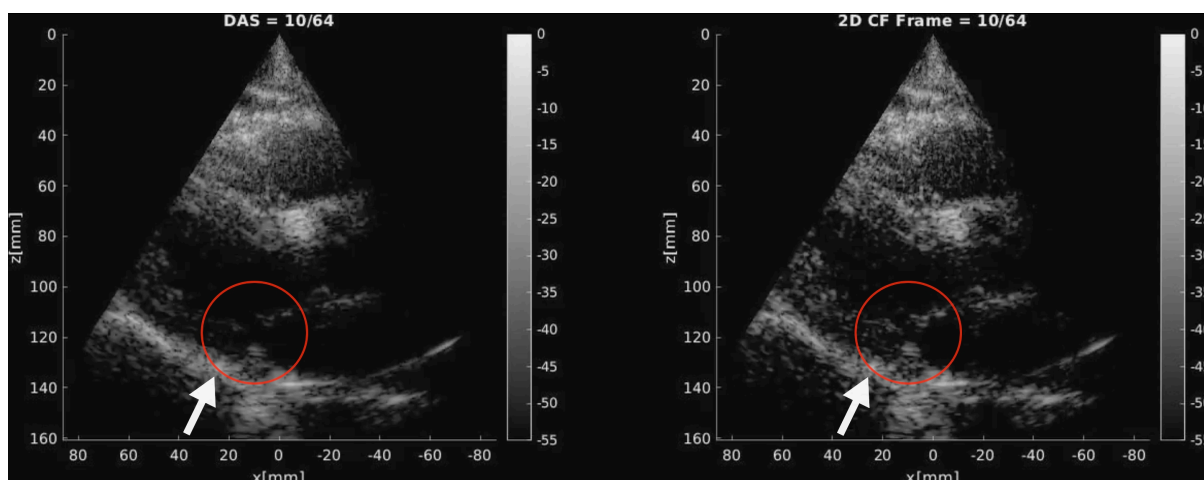
Figure 4.2: Ultrasound frame that indicates an improvement in 2D CF (right) over DAS (left).

A second example from another patient can be seen in figure 4.2. The circled structure in the right frame is both brighter and more detailed than the structure in the left frame. This is another example where the 2D CF yields a significant improvement.
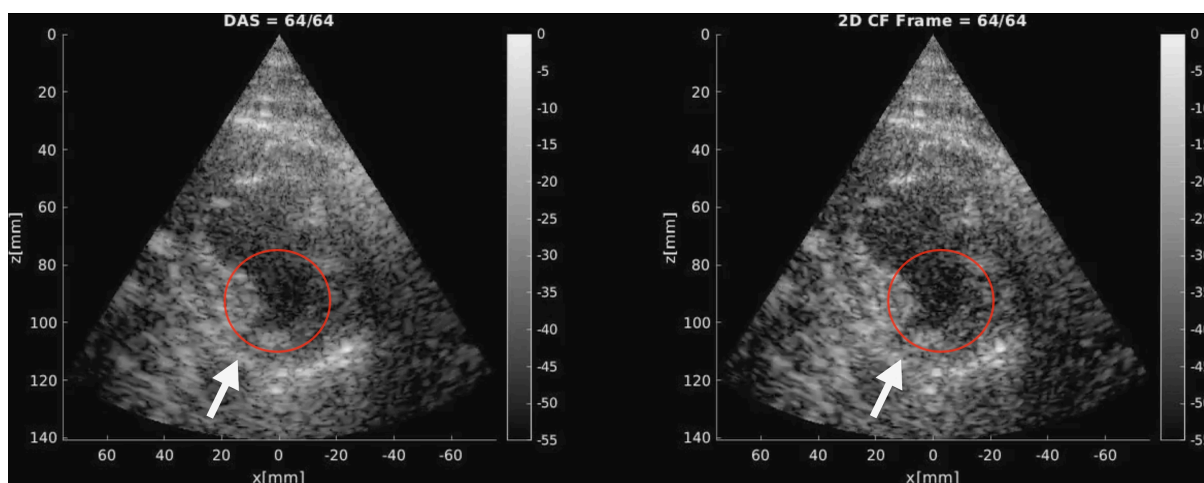
Figure 4.3: Ultrasound frame that indicates an improvement in 2D CF (right) over DAS (left).

For some frames, the 2D CF does a good job in reducing the noise. Noise reduction, specifically in the heart cavity, can lead to crisper borders. Figure 4.3 illustrates a case where the reduction in cavity noise for the 2D CF image leads to clearer borders. The 2D CF image on the right has sightly less noise, and some of the borders at the bottom of the circle are easier to see.

The videos that were placed in the green category all had the majority of the frames

showcasing an improvement for the 2D CF relative to the DAS. It was not enough that only one or two frames showed a clear improvement.

4.1.2   Yellow category - videos with little to no improvement

The videos in the yellow category did not show as clear and improvement with the 2D CF as the videos in the green category. For some of the videos, it was not easy to determine which was better, the DAS or the 2D CF image. In some cases, the videos would be very similar and difficult to distinguish. In others, the 2D CF image might have some more details than the DAS in a few frames, but not in enough frames to conclude that there was significant improvement.
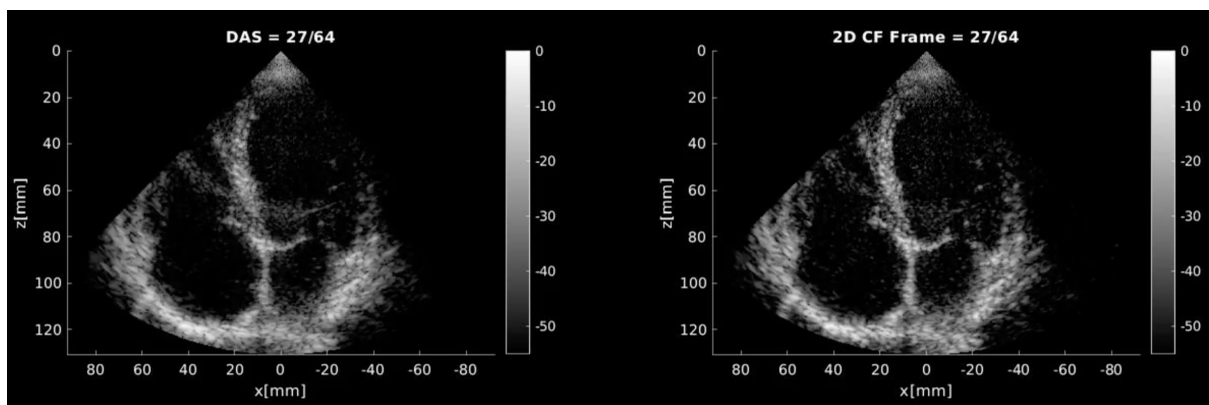
Figure 4.4: Ultrasound frame that illustrates similarity between the image quality for DAS and the 2D CF.

The frames in figure 4.4 are an example of two images that are very similar. Videos that had large portion of the frames exhibiting such similarities were placed in this category.
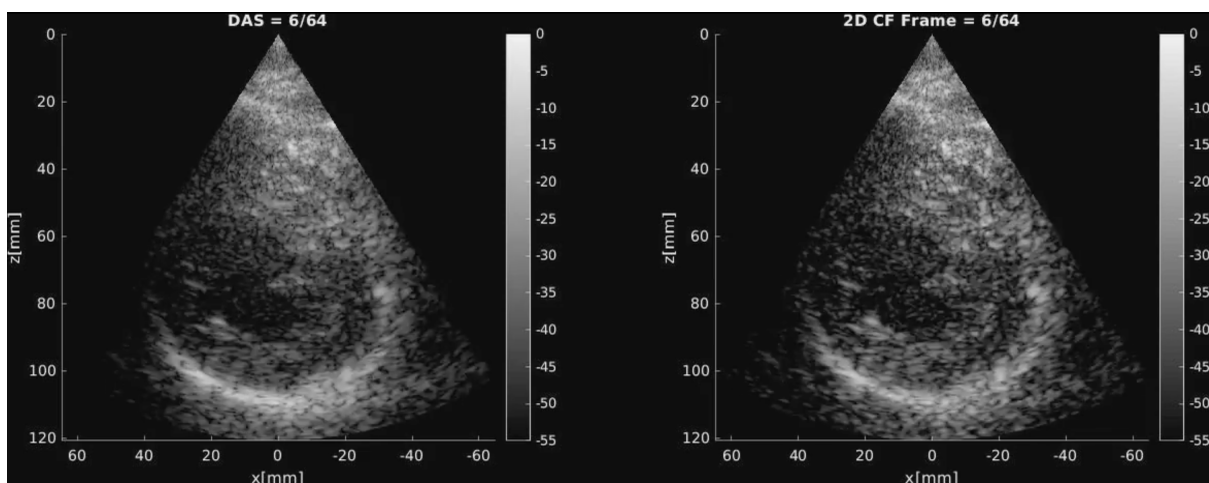
Figure 4.5: Ultrasound frame that indicates two similar, low quality images.

Figure 4.5 shows another type of video that was placed in this category. The image quality is over all quite poor, which makes it more difficult to pick out small nuances in the quality.

4.1.3   Overview of the initial assessment

In total, 45 videos were assessed in the manner explained above. 30 of the 45 videos were deemed significantly better for the 2D CF, and placed in the green category. 15 were given the colour yellow, which indicates that the videos showed little to no improvement for the 2D CF. No videos were placed in the red category, meaning that no videos indicated a decrease in image quality for the 2D CF compared to the DAS. This is summarized in table 4.1.

Colour	Meaning	Number of videos in category	Percentage of total videos
Green	The 2D CF image shows a clear improvement compared to the DAS image.	30	66.7%
Yellow	The 2D CF image shows little to no improvement compared to the DAS image	15	33.4%
Red	The DAS image shows a clear improvement compared to the 2D CF image.	0	0%

Table 4.1: Colour coding and number of videos in each category.

The main and most interesting result from this step in the data inspection is what percentage of the videos show an improvement for the 2D Coherence Factor images, and which do not. The fourth column in table 4.1 indicates these percentages.

This initial examination indicates that 66.7% of the videos show an improvement for the 2D CF. 33.4% of the videos show a weak improvement or none at all. None of the videos show a decrease in image quality when the 2D Coherence Factor is applied.

4.2   Examination of Data from Aperture Energy Maps

As illustrated in the excel sheet in figure 3.7, after all the videos were studied, the maps of the aperture energy were studied. The second style of aperture map, with the normalization performed for all beam individually, was used. The style of aperture energy

map is illustrated in figure 3.5. A small comment on the nature of the aperture energy was noted in a spreadsheet. This comment would indicate if the blockage was non-existent, in azimuth alone, in elevation alone or a mix of elevation and azimuth.
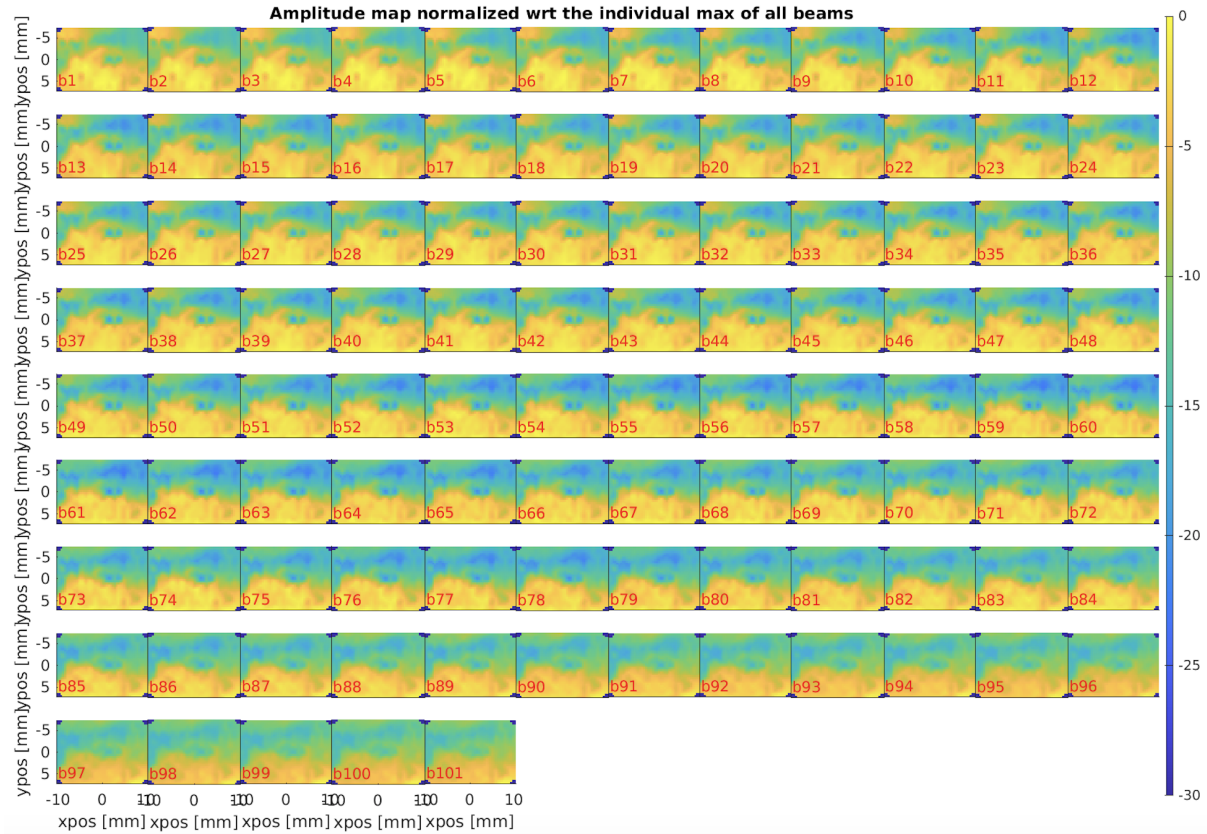
Figure 4.6: Aperture energy map displaying a blockage in the elevation direction.

Figure 4.6 illustrates how a blockage that predominantly varies in elevation direction might look like. The blockage is restricting a large amount of energy, 25 dB at most. The geometry of the blockage variation is quite similar for all beams in the case of figure 4.6.
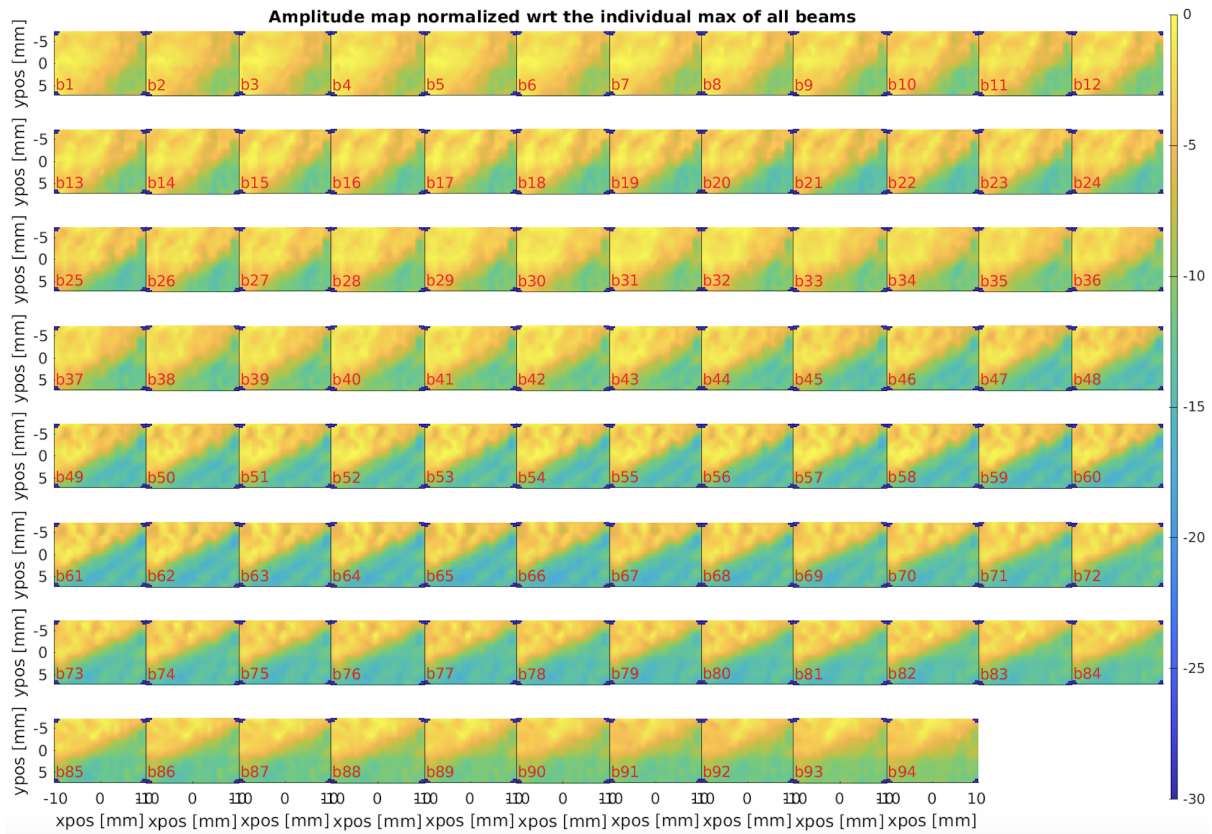
Figure 4.7: Aperture energy map displaying a blockage in both azimuth and elevation direction.

Figure 4.7 is one of many aperture energy maps that has a form of aperture blockage in both directions. This could often be a corner like the illustration shows. This aperture energy map also has quite a powerful blockage, with the blocked elements receiving between 15 and 20 dB less than the other elements.

Not all aperture maps have blockages as prominent as the two previous cases. The aperture energy map in figure 4.8 is an example of this. The range of energy values is narrower, as the blockage is at most 10 dB less than the maximum values. These types of aperture maps are more difficult to categorize, as the variation in the blockage geometry is weaker. The majority of the aperture maps were of this nature, with weak blockages.
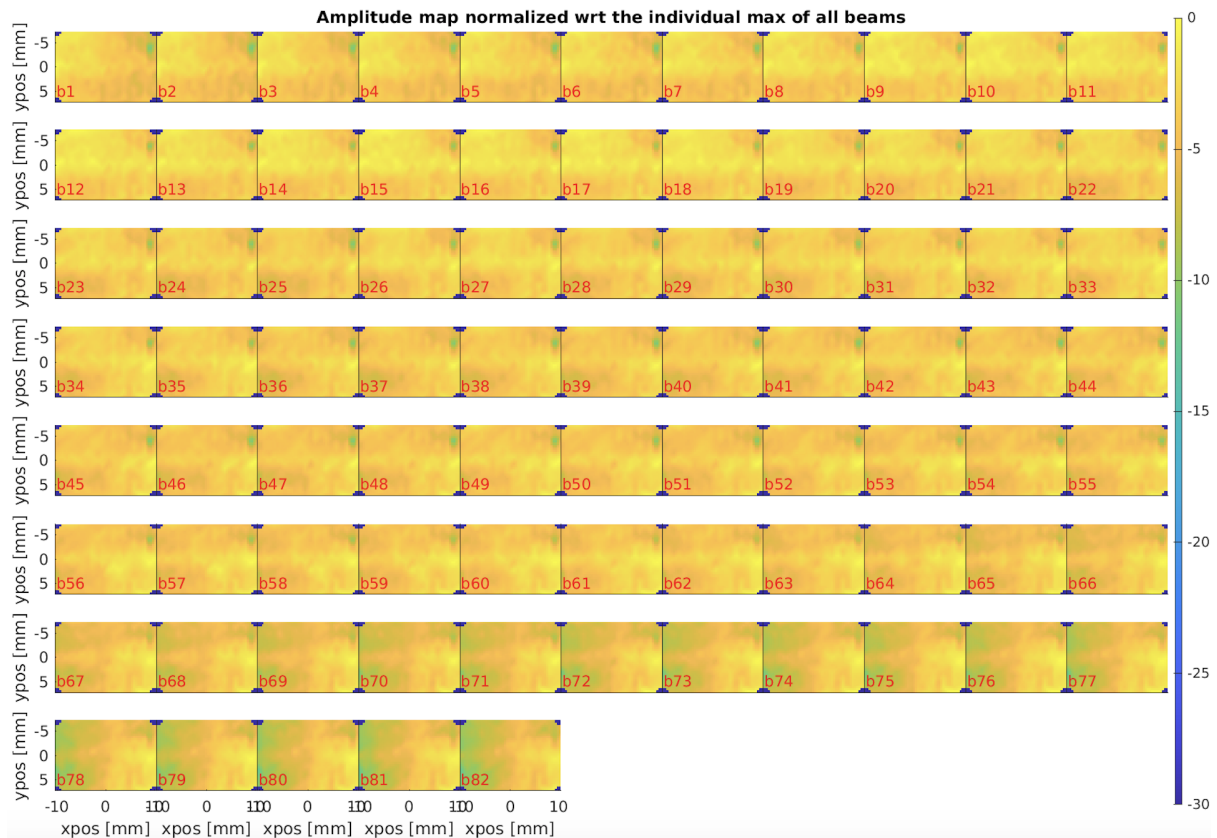
Figure 4.8: Aperture energy map displaying a weaker blockage.

Initially, the aperture maps were studied with a disregard for the quality of the video, i.e if the video was colour coded green or yellow. From the spreadsheet indicating the nature of the blockages, the table in 4.2 was created. The table indicates that most of the aperture blockages vary in both azimuth and elevation direction simultaneously. A total of 79.9% of the videos have some form of aperture blockage in the azimuth direction, and a larger portion, 95.55% have a blockage in the elevation direction.

Type of blockage	Number of videos with this type of blockage	Percentage of videos with this type of blockage
None	0	0%
Azimuth	2	4.44 %
Elevation	9	20 %
Both azimuth and elevation	34	75.55 %

Table 4.2: Type of aperture blockage for all 45 videos.

Another number of interest is the percentage of blocked elements for each video. As mentioned in section 3.3.6 on the aperture energy maps, two graphs representing the

percentage of blocked elements per beam were created. This was done by choosing a threshold of -12dB, and categorizing all elements with a received signal energy less than the threshold as a blocked element. For every video, a mean percentage of blocked elements was calculated, using equation 3.7. The average of these percentages for all 45 video is found to be 6.75%. This implies that, in average, 6.75% of the elements are blocked across all 45 videos.

In order to somehow summarize the connection between performance of the algorithm and the aperture maps, the number of videos exhibiting aperture blockage variations in either azimuth, elevation or a mix of these two was calculated for both colour groups. The results from these two groups will now be presented consecutively.

4.2.1   Aperture energy blockages in the green category

30 videos indicate an improvement for the 2D Coherence Factor. The distribution of these videos within the different aperture blockage categories can be seen in table 4.3

Type of blockage	Number of videos with this type of blockage	Percentage of videos with this type of blockage
None	0	0%
Azimuth	2	6.66%
Elevation	9	30 %
Both azimuth and elevation	19	63.33 %

Table 4.3: Distribution of videos displaying improvement by 2D CF and their aperture blockages.

The data in table 4.3 implies that 93.33% of the videos that are improved by the 2D CF have some form of blockage in the elevation direction. Simultaneously, 69.99% of the videos that are improved have a blockage of some type in the azimuth direction.

The mean percentage of blocked elements across the 30 videos in this category is 5.86%, which is a bit lower than the percentage for all 45 videos, at 6.75%.

4.2.2   Aperture energy blockages in the yellow category

There are 15 videos that do not show any significant improvement in the 2D CF images. Table 4.4 shows the aperture blockage distribution for these videos. All of the aperture

energy maps in this category display a variation in both the azimuth and elevation direction.

Type of blockage	Number of videos with this type of blockage	Percentage of videos with this type of blockage
None	0	0 %
Azimuth	0	0 %
Elevation	0	0 %
Both azimuth and elevation	15	100 %

Table 4.4:   Distribution of videos displaying no improvement by 2D CF and their aperture blockages.

The mean percentage of blocked aperture elements for these 15 videos is 9.2%. This number is higher than the mean for both the green category and also for all 45 videos.

4.3   Examination of Data from Image Views

The third and final approach to organizing and studying the data was done with the type of imaging view in focus. The same statistics that have been presented in the two previous steps were used, but videos were placed into 5 groups depending on image view type and then analyzed according to this grouping. The idea behind this step was to examine if the 2D Coherence Factor performs any different for the various imaging views. There are 9 videos in every group, and the percentages and numbers presented within each group are calculated relative to the 9 videos within that group.

4.3.1   PLAX: Parasternal Long Axis
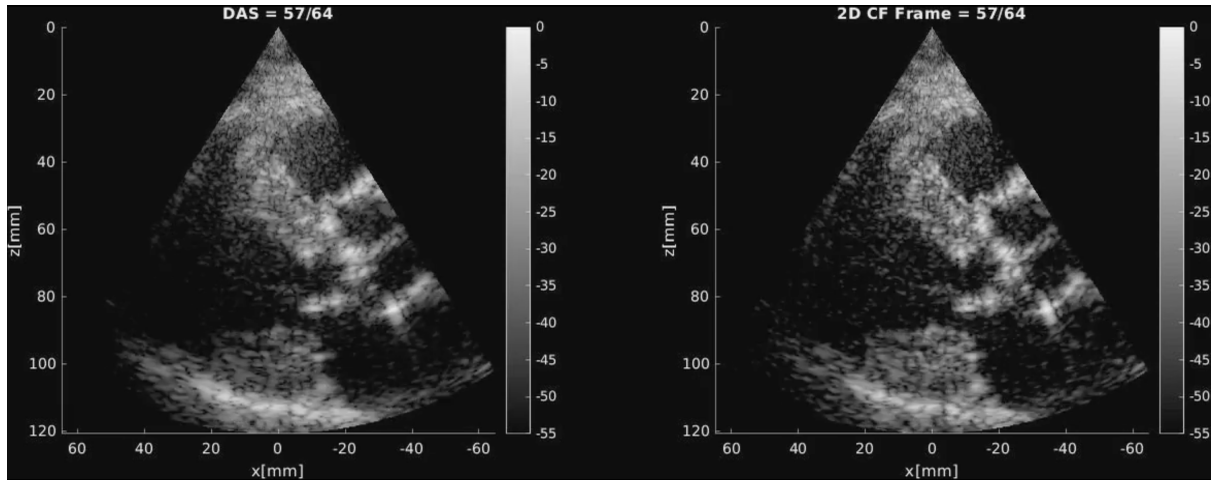
Figure 4.9: Parasternal long axis view of the heart.

Figure 4.9 is one frame in an image sequence taken with the parasternal long axis view of the heart. The videos from this category all show improvement for the 2D Coherence Factor. This can be seen in table 4.5

Colour	Number of videos in category	Percentage of total videos
Green	9	100 %
Yellow	0	0 %

Table 4.5:   PLAX videos and their image quality.

The distribution of the PLAX videos within the blockage categories is illustrated in table 4.6.

Type of blockage	Number of videos with this type of blockage	Percentage of videos with this type of blockage
None	0	0 %
Azimuth	1	11.1 %
Elevation	3	33.3 %
Both azimuth and elevation	5	55.5 %

Table 4.6:   PLAX videos and aperture energy blockages.

The mean percentage of blocked elements for the PLAX view is 0.67%. This number is low compared to the global average over all videos, which is 5.86%.

4.3.2   PSAX: Parasternal Short Axis

The parasternal short axis view is related to the parasternal long axis view, but looks quite different. An example of a DAS and 2D CF image frame for the PSAX view can be seen in figure 4.10. In contrast to the PLAX view, this view contains videos from both image quality categories. This can be seen in table 4.7.
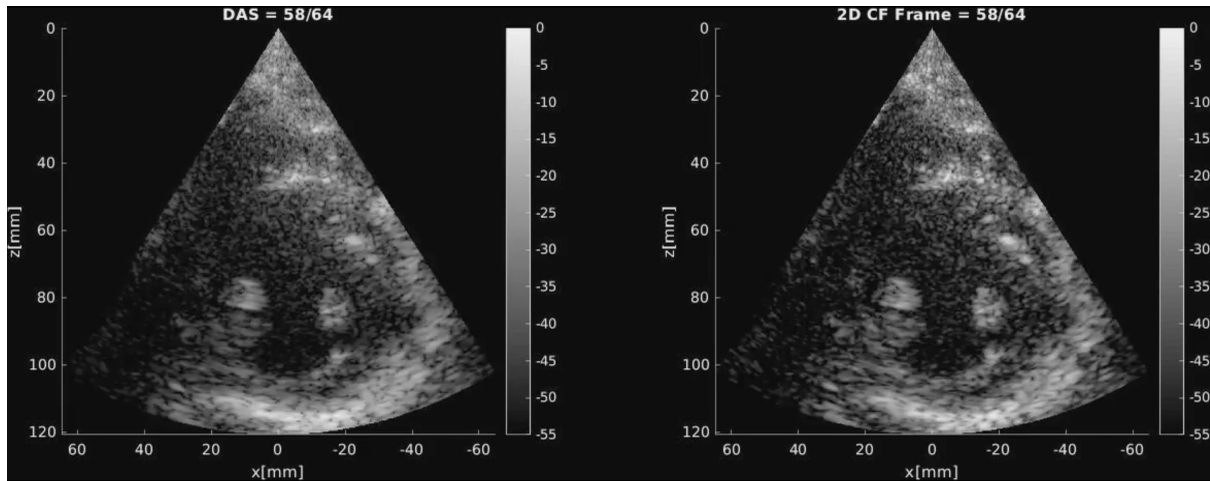
Figure 4.10: DAS and 2D CF frame for the PSAX view of the heart.

Colour	Number of videos in category	Percentage of total videos
Green	7	77.8 %
Yellow	2	22.2 %

Table 4.7: PSAX videos and their image quality.

Videos in this category either have blockages in the elevation direction alone or in both azimuth and elevation directions. This is summarized in table 4.8.

Type of blockage	Number of videos with this type of blockage	Percentage of videos with this type of blockage
None	0	0 %
Azimuth	0	0 %
Elevation	2	22.2 %
Both azimuth and elevation	7	77.7 %

Table 4.8: PSAX videos and their aperture energy blockages.

The mean percentage of blocked elements for this view is just slightly larger than for the PLAX, with an average of 0.87% of the elements blocked.

4.3.3   A4C: Apical Four Chamber
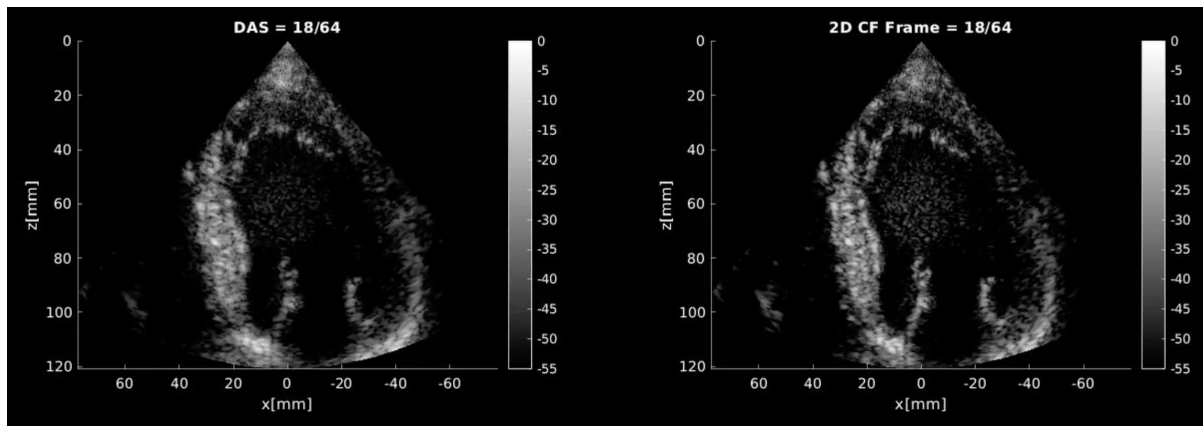
Figure 4.11: DAS and 2D CF frame from A4C view.

Two imaging frames taken with an apical four chamber view can be seen in figure 4.11. The images taken with the A4C view were less noisy and in general clearer relative to the rest. The number of videos in the green and yellow categories for the apical four chamber view is given in table 4.9.

Colour	Number of videos in category	Percentage of total videos
Green	5	55.5 %
Yellow	4	44.4 %

Table 4.9:   A4C videos and their image quality.

The distribution of aperture blockage types for the A4C view is the same as for the PSAX, as indicated in table 4.10.

Type of blockage	Number of videos with this type of blockage	Percentage of videos with this type of blockage
None	0	0 %
Azimuth	0	0 %
Elevation	2	22.2 %
Both azimuth and elevation	7	77.7 %

Table 4.10:   A4C videos and their aperture energy blockages.

The mean percentage of blocked elements for the apical four chamber view is significantly higher than for the PLAX and the PSAX views. The average is 10.44%.

4.3.4   A2C: Apical Two Chamber
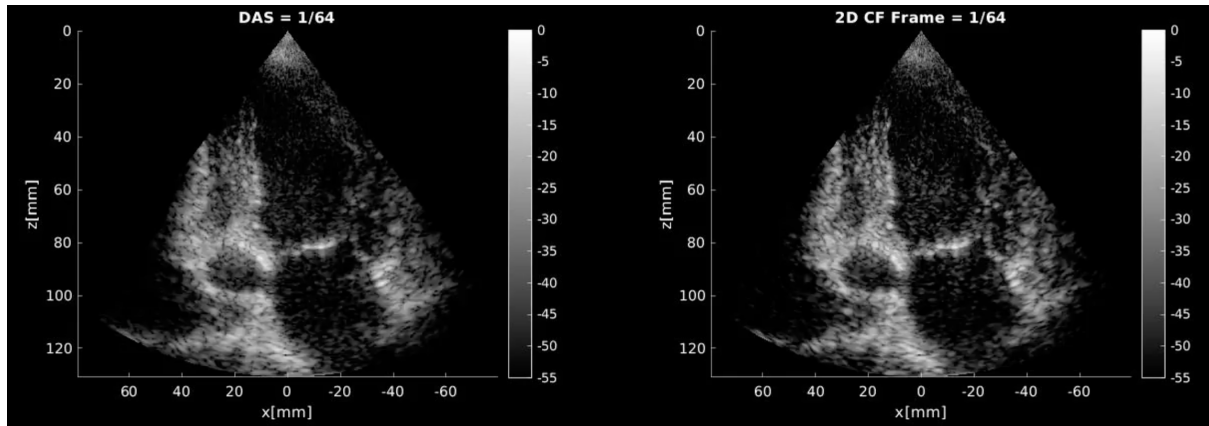
Figure 4.12: A DAS and 2D CF frame for the A2C view of the heart.

Figure 4.12 shows a DAS frame and a 2D CF image frame for the apical two chamber view. The number of videos from the green and yellow category can be found in table 4.11.

Colour	Number of videos in category	Percentage of total videos
Green	3	33.3 %
Yellow	6	66.6 %

Table 4.11: A2C videos and their image quality.

Table 4.12 indicates the nature of the aperture energy blockages for the 9 videos in this category.

Type of blockage	Number of videos with this type of blockage	Percentage of videos with this type of blockage
None	0	0 %
Azimuth	0	0 %
Elevation	2	22.2 %
Both azimuth and elevation	7	77.7 %

Table 4.12: A2C videos and their aperture energy blockages.

The mean percentage of blocked elements for this view is similar to the A4C at 10.11% of the elements blocked.

4.3.5   ALAX: Apical Long Axis
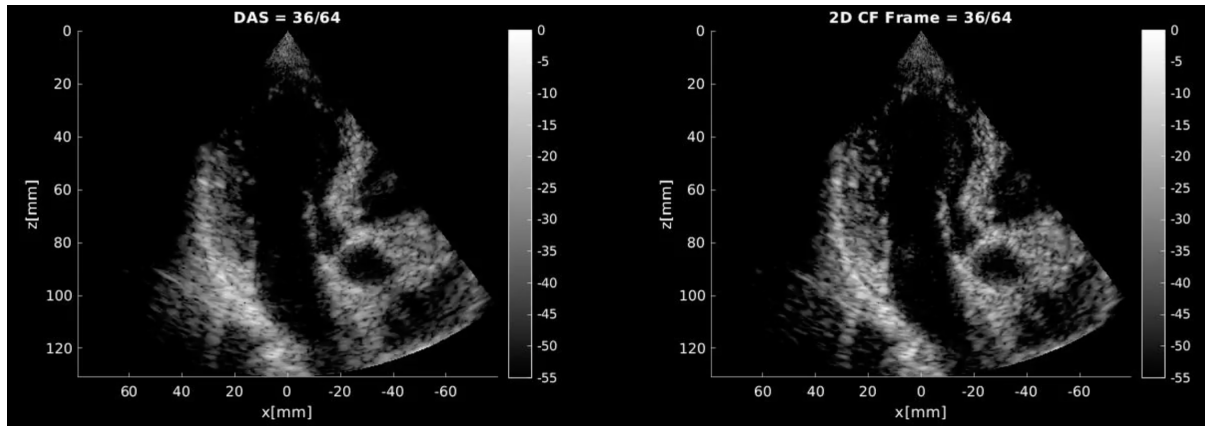
Figure 4.13: A DAS and 2D CF frame for the ALAX view of the heart.

The last view is the apical long axis view. Two frames with this view can be found in figure 4.13. The number of videos in the two image quality categories is indicated in table 4.13.

Colour	Number of videos in category	Percentage of total videos
Green	6	66.6 %
Yellow	3	33.3 %

Table 4.13:   ALAX videos and their image quality.

Table 4.14 shows the distribution of aperture blockage types among the 9 videos in this category.

Type of blockage	Number of videos with this type of blockage	Percentage of videos with this type of blockage
None	0	0 %
Azimuth	1	11.1 %
Elevation	0	0 %
Both azimuth and elevation	8	88.8 %

Table 4.14:   ALAX videos and their aperture energy blockages.

The mean percentage of blocked elements for the apical long axis view is the highest of all five views. 11.66% of all elements are blocked on average across all 9 videos.

4.3.6   Summary of image view statistics

Table 4.15 Summarizes the statistics and metrics presented in this section.

Image view name	Image quality category		Type of blockage			Average no. of blocked elements.
	Green	Yellow	Azimuth	Elevation	Azimuth and elevation	
PLAX	9	0	1	3	5	0.67
PSAX	7	2	0	2	7	0.87
A4C	5	4	0	2	7	10.44
A2C	3	6	0	2	7	10.11
ALAX	6	3	1	0	8	11.66

Table 4.15:   Summary of statistics regarding image views.

5 Discussion

In this chapter, the results presented in chapter 4 of this thesis will be discussed. The discussion will be divided into three parts, following the style in which the results were presented in chapter 4.

It is important to note that the comparisons in this thesis are between the 2D Coherence Factor and the delay-and-sum (DAS) images. It could have been possible to compare the 2D Coherence Factor with the Coherence Factor. The DAS was chosen over the Coherence Factor due to the fact that it is perceived as a better reference. DAS is the current technique used in the average ultrasound scanner, and it therefore made more sense to compare with the DAS images. In addition, there is not a clear consensus on whether the Coherence Factor improves image quality across the board. Weaknesses like the dark region artefacts examined by Rindal et al. [29] have been found, and the DAS was therefore a safer reference technique.

5.1 Preliminary Examination of Image Quality

This first stage focused mostly on organizing the data into categories depending on how well the 2D Coherence Factor performed compared to the delay-and-sum beamforming algorithm. No videos showed the DAS algorithm performing better than the 2D Coherence Factor, and the majority of the videos showed significant improvement in the images where the 2D Coherence Factor was applied. This preliminary examination would indicate that the 2D CF algorithm does improve the image quality, and that, most importantly, it doesn't deteriorate the quality compared to the standard DAS beamforming technique.

However, these results need to be taken with a grain of salt, as the categorization of these videos was merely visual and not based on any quantifiable parameters. The videos were also only observed by one person. There is a possibility that there is some bias in these results, as the type of imaging postprocess was not hidden from the observer. Another possibility is that there were videos from too few patients to examine, and that the results do not represent the majority of ultrasound image acquisitions. Still, with these sources of inaccuracy in mind, it can still seem that the 2D Coherence Factor is a real improvement over conventional delay-and-sum imaging.

5.2   Examination of Data from Aperture Energy Maps

This section is of high importance, as some of the motivation for wanting to create the 2D Coherence Factor was to account for variations in the nature of the aperture blockages. The 2D Coherence Factor uses a window to be able to pick out spatial variations in the aperture energy. The window is in elevation direction, and one central question for this algorithm is whether it performs better for aperture energy blockages in elevation direction than it does for other types of blockages. The data in the results section was therefore evaluated based on what type of aperture energy blockage was present.

The videos were considered based on their colour category. The first category to be examined was the videos in which the 2D Coherence Factor performed better than the DAS images, i.e the green category. 30 videos were placed in this category, and of these videos, as many as 93.33 % of the aperture maps had some form of blockage in elevation direction. This could suggest that there is a correlation between instances where the 2D CF performs well and aperture energy blockages in elevation direction. Simultaneously, 69.99 % of the videos in this category have a form of blockage in the azimuth direction. This number is also high, and could indicate that the algorithm performs well for any type of aperture energy map. It is also necessary to remember the distribution of aperture energy maps over all 45 videos. The fact that so many of the videos have blockages in both directions, leads to a large number of videos with an elevation blockage ending up in the green category. It is therefore more correct to look at the numbers in another way. Out of all the 45 videos in total, 43 of these had some form of aperture energy variation in elevation direction, and 36 videos had a form of azimuth aperture energy variation. The statistics from section 2 of the results chapter are organized to reflect this in table 5.1

Blockage type	Total	Green	% in green	Yellow	% in yellow
Azimuth	36	21	58.33	15	41.67
Elevation	43	28	65.12	15	34.89

Table 5.1: Aperture energy blockage types and how they are split into colour categories.

There are in total 36 videos that have aperture energy maps varying in azimuth direction, and 43 videos with aperture maps varying in elevation direction. It is important to remember that these groups include both the aperture energy maps varying in both

directions and the aperture maps varying in only one. Table 5.1 illustrates that a larger portion of the videos with energy blockages in elevation direction end up in the green category, 65.12% to be precise. In contrast, 58.33% of the videos with an azimuth blockage end up in the green category. This indicates that there is a tendency of videos with a blockage in elevation direction to be perceived as good quality videos when the 2D CF is applied. This could indicate that the CF 2D performs slightly better for blockages in elevation direction. However, there are sources of error in this analysis, and the findings could be circumstantial.

A different angle to consider is the fact that the yellow category consists solely of videos with aperture energy blockages in both azimuth and elevation, as expressed in table 4.4. This further implies that all the videos that have an aperture blockage in only one direction are a part of the green category. Percentage wise, this means that the green category has 63.33 % of videos with a mixed aperture map and 36.66 % of videos with a simple aperture map. Simple in this context means that the energy only varies in one direction. The yellow category has 100 % of videos with mixed aperture blockages. Judging by these statistics, it appears that the 2D Coherence Factor performs better with simple aperture map blockages. Nevertheless, these statistics are based on only 11 videos, which might be too few to be accurate. Also, there are very few videos with only azimuth blockages (only 2) making it difficult to draw conclusions for this type of aperture blockage.

Another metric that was presented is the mean percentage of blocked elements for each scan. The average for all 45 videos was found to be 6.75 % of the elements. The average for the 30 videos in the green category was 5.86 % while the average for the yellow category was 9.2 %. This indicates that the 2D Coherence Factor works better when there are fewer blocked elements. Having said that, there is an uncertainty in the calculation of the number of blocked elements. This number is based on a set threshold value for all images, and this threshold value is not adapted to the individual videos.

The mean percentage of blocked elements should be considered for each type of aperture energy blockage, to determine if there is any correlation between the different types of energy blockages and the number of blocked elements they have. This is summarized in table 5.2. This table outlines how the average percentage of blocked elements varies with the different aperture blockage types. What is clear from this table, is that the videos

with elevation-only aperture blockages have a higher amount of blocked elements than the azimuth videos. Something interesting to note is the trend for the videos that have aperture blockages in both directions. Across all 45 videos, these have an average of 6.14% of their elements blocked. The videos that are placed in the green category however, have a lower mean number of blocked elements (3.73%) than the videos that are placed in the yellow category (9.2%). This further strengthens the indication that the 2D CF performs better for images with few blocked aperture elements.

Video category	Azimuth blockage mean	Elevation blockage mean	Elevation- and azimuth blockage mean
All videos(45)	1%	10.33%	6.14%
Green videos(30)	1%	10.33%	3.73%
Yellow videos(15)	-	-	9.20%

Table 5.2: Aperture energy blockage types and how they are split into colour categories.

Furthermore, the types of blockages that are contributing to lowering the mean amount of blocked elements for the green category, are the azimuth blockages and the blockages in both directions. The videos with elevation-only blockages have a mean amount of blocked elements of 10.33% and this is the blockage type with the highest amount of blocked elements. This could imply that the videos that have a tendency to do well with the 2D CF are a) videos with a simple aperture elevation blockage or b) videos with a low amount of blocked elements. It is difficult to draw a conclusion regarding the videos with the azimuth-only blockages. There are so few, so the reason they are performing well with the 2D CF could be their low mean value, that the blockage type is simple or something arbitrary.

In summary, the study of the data in light of which aperture energy blockage is present reveals some patterns. The 2D CF could possibly perform better for blockages in elevation direction, for simple blockages in one direction only and for image acquisitions where there are few blocked aperture elements. In addition to the uncertainty regarding the mean of blocked elements and the uncertainty in the grouping of the videos into the green and yellow category, there is an uncertainty in the analysis of the aperture maps. The categorization of the aperture energy maps was only performed by one person. The nature of the blockages was sometimes tricky to determine, as there could be multiple types of blockages with very different strengths.

5.3   Examination of Data from Image Views

When gauging the performance of an ultrasound processing tool, it can be of interest to examine whether this tool works better for different imaging views. Section 4.3 of the results chapter presented the statistics for the videos according to type of image view. There are 5 different types of views, and each image view group has 9 videos.

The first view considered is the parasternal long axis (PLAX) view. The 2D Coherence Factor performs well for the PLAX images, as all 9 videos in the category are so called "green videos", i.e all videos show a significant improvement when the 2D CF is used. In addition, the mean percentage of blocked elements is very low for this view, the lowest for all the views, at 0.67% of elements on average. When it comes to type of aperture blockages, the PLAX view has 88.8 % of videos with some kind of aperture blockage in the elevation direction and 66.6% of videos with some kind of blockage in the azimuth direction. Also, the view group consists of 4 videos (44.4%) with a simple aperture blockage, and 5 videos (55.5%) with a mixed aperture blockage. The PLAX view is the view with the highest number of videos showcasing a simple aperture blockage pattern.

The second view is the parasternal short axis (PSAX) view. This view also has a large portion of images that are improved by the 2D Coherence Factor. 77.8% of the videos in the PSAX view group are categorized as green videos. The mean percentage of blocked elements is very low also for this view, at 0.87%. The aperture energy blockage distribution consists of 77.7% of videos with a blockage in azimuth, 100% of videos with a blockage in elevation and 22.2% of videos with a simple type of blockage. There are two videos with a simple aperture blockage in this category, both with blockages in elevation.

The apical four chamber (A4C) view was analyzed next. This group has 5 videos (55.5%) from the green category and 4 videos (44.44%) from the yellow category. The average percentage of blocked elements is a lot higher for this category, at 10.44%. The distribution of aperture blockage types is identical to that of the PSAX view, with 77.7% of videos with a form of azimuth blockage, 100% of videos with a type of elevation blockage and 22.2% of videos with a simple elevation blockage.

The apical two chamber (A2C) view includes the largest percentage of videos from the yellow group across all views. 6 videos (66.6%) are from the yellow group and 3 videos

(33.3%) are from the green group. The average amount of blocked elements is high also for this group, at 10.11%. The distribution of the aperture blockages is the same as for the PSAX and the A4C view.

The last view to be considered is the apical long axis (ALAX) view. This grouping consists of 6 videos from the green category (66.66%) and 3 videos from the yellow category (33.3%). The average percentage of blocked elements for the ALAX is the highest for all the views at 11.6%. The group consists of 88.8% of videos with a form of blockage in elevation, 100% of videos with a form of blockage in azimuth and 11.1% of videos with a simple blockage type, in this case in azimuth direction.

After comparing the five imaging views there are a few things to note. The PLAX view and the PSAX view have the largest amount of videos in the green category. The also have the lowest amount of blocked elements on average, and this average is substantially lower than for the three other views. They are the two views that do best with the application of the 2D Coherence Factor. This could support the theory that the 2D Coherence Factor works best with few blocked elements on the aperture. This trend is not consistent throughout all views though. The average amount of blocked elements jumps from under 1 percent for the PLAX and the PSAX up to over 10 percent for the A4C, A2C and the ALAX. The number of videos belonging to the green group per view however, does not decrease proportionally. For the ALAX, the image view group with the largest percentage of blocked elements, 66.6% of the videos are from the green group. This is only 11.1% lower than for the PSAX group. For the other two groups, the A4C and the A2C, the amount of green videos in the categories are 5 and 3 respectively.

It seems safest to conclude that the 2D Coherence Factor works best for the PLAX group, and also good for the PSAX and the ALAX group. The reason why the algorithm is working well with the PLAX and the PSAX group could be down to the low amount of blocked elements. It is more tricky to explain the behaviour of the three other categories. There could be too few videos to see the actual trends in the data, and a larger database of patient data could yield results more consistent with the results for the PLAX and the PSAX groups.

Another suggestion that was made in the previous section was whether the 2D CF performs better on the videos with simple aperture blockages. This observation is indeed consistent

with the performance of the PLAX, as the view group that performs the best quality-wise with the 2D Coherence Factor, is the group with the largest amount of videos with simple aperture blockages. 4 out of 9 videos for the PLAX group have a simple aperture blockage. This could indicate that videos with aperture blockages in either azimuth or elevation perform best with the 2D CF. For the other four groups, there is no such trend to observe. The groups have quite a similar amount of videos with simple blockages, the PSAX, A4C and A2C all have 2 videos with a simple aperture blockage, and the ALAX has one video with a simple aperture blockage. The fact that there is a significant difference in quality between say the PSAX and the A2C (7 green videos vs 3 green videos) but no difference in the number of videos with a simple aperture blockage (2 in both cases) could also indicate that the 2D Coherence Factor does not work any better with the simple aperture blockages. The trends we are seeing could be circumstantial due to there only being 9 videos in each category.

When it comes to the sources of uncertainty, they might be even larger than anticipated. The PSAX view is expected to have more blocked elements than the data is indicating. The nature of the image acquisition usually means that part of the aperture gets blocked by a rib. This seems to be the case in the example image of the PSAX view in chapter 4, figure 4.10. The left side of the images appears to have quite large blockages. These blockages are not reflected in the data, as the highest amount of blocked elements for a video is 5 % and most of the videos have an average blockage of 0%. This strengthens the suspicion that either the aperture energy maps are not as accurate as hoped, or that the calculation of the number of blocked elements including the choice of threshold is inaccurate.

To summarize, the PLAX seems to perform the best, as all videos from this view are improved significantly by the 2D Coherence Factor. The PLAX is followed by the PSAX with 7 out of 9 videos in the green category. The PSAX is then closely followed by the ALAX at 6 videos in the green category, the A4C with 5 videos in the green category and lastly by the A2C with only 3 videos in the green category. The two best performing views have a much lower amount of blocked elements than the three views that perform the worst. However, there are too few videos in each category to determine if these trends are representative or merely random.

5.4   Overview of the Results

Returning to the main hypothesis; whether the 2D Coherence Factor performs best for blockages in elevation direction. It is hard to say something definite, but there is an indication that this hypothesis could hold. All the videos with an elevation-only aperture energy blockage are placed in the green category. This is highlighted in table 5.2. Also, when splitting the 45 videos into two aperture blockage categories like in table 5.1, it is seen that a larger amount of videos with a form of elevation direction blockage end up in the green category, compared to the videos with an azimuth direction blockage. This could indicate that the use of the sliding window in elevation really is able to pick out variations better, and that this improves the image quality when the images have a blockage in elevation.

Another tendency that has become apparent during the analysis of the results is the amount of blocked elements and how this effects the performance of the 2D Coherence Factor. It seems that the amount of blocked elements affects how well the 2D Coherence Factor performs. Specifically, it seems like the lower the amount of blocked elements, the better the 2D Coherence Factor performs. This can be seen in the statistics for the image views, with the two best performing views having the lowest amount of blocked elements. It is also apparent when comparing the mean amount of blocked elements for the green and yellow group, with the green group having 3.35 % less blocked elements on average. Table 5.2 also outlines how, among the videos with the blockages in both dimensions (column 4), the videos that end up in the green category have a lower mean than the videos that end up in the yellow category. From the table we can read that this difference is 5.47 %. This is interesting, as the 2D CF is aimed at improving image quality in the presence of aperture blockages. The reason for the algorithm performing so well even without the presence of blockages could be the smoothing effect of the algorithm. By dividing the aperture into smaller sub-apertures corresponding to the size of the windows, and then combining these together into one has a smoothing and noise reducing effect. Each window represents a smaller part of the aperture, which leads to the beam widening in elevation direction. This widening effect can lead to more information being picked up than with a narrower beam. Every contribution from the windows can be viewed as a weight. When these weights are combined, an averaging effect is achieved, and the signal

to noise ratio is improved.

The sources of uncertainty have been mentioned throughout the discussion, but it is important to note that the results in this paper are by no means conclusive. This is a pilot study, and its goal is to determine whether it is justified to continue refining and testing this algorithm. In order to make decisive conclusions on the 2D Coherence Factors performance, a much larger study is necessary. However, the results in this paper are positive, and indicative of there being some improvement in the image quality of echocardiograms when the algorithm is applied.

6 Conclusion

This paper has analyzed 45 videos from 9 different patients in order to establish if an ultrasound post-processing tool called the 2D Coherence Factor has a positive impact on the image quality. Over 2200 ultrasound images were studied using a three step method in order to judge the performance of the 2D Coherence Factor. The videos were split into two categories depending on how the 2D CF altered the image quality. The green category videos showed a real improvement with the 2D CF and the yellow category videos showed no change/a slight improvement with the 2D CF. There were 30 videos that showed a significant improvement, and were placed in the green category. 15 videos showed no real difference or possibly a slight improvement for some frames, and were placed in the yellow group. No videos were deemed to be poorer in image quality after the application of 2D Coherence Factor, so there was no need for a third category.

The hypothesis was connected to the type of aperture energy map blockage, and specifically wanted to establish if the 2D Coherence Factor performed better when the aperture blockage was in elevation direction. The study of the aperture maps was therefore an important component in the generation of the results. The results indicate that the 2D Coherence Factor does perform slightly better if the aperture blockage is in elevation direction. Of the 9 videos with a simple aperture blockage in elevation, 100% of these are placed in the green category. In addition, there are 43 videos in total that showcase an aperture blockage that varies in elevation direction in some form. Of these videos, 65.12% of them are placed in the green category.

When it comes to the videos with the azimuth only blockage, it is hard to tell as there are only 2 videos with pure azimuth blockages. Like the elevation blockages, 100% of the azimuth only blockage videos are placed in the green category. Also, of all the videos with some form of azimuth blockage, 58.33% of them end up in the green category. This is a bit less than for the elevation videos, but still larger than 50%. This could indicate that the 2D Coherence Factor improves the azimuth videos and the elevation videos to the same degree, but this is harder to establish as there are too few videos.

In addition to improving the images with significant blockages, the 2D CF algorithm seems to improve images with few blocked aperture elements to a larger degree than it

improves images with a high amount of blocked elements. The image view group that performs the best has the lowest amount of blocked elements. Also, the green group, which contains the videos that show improvement by the 2D Coherence Factor, has a lower average amount of blocked elements than the yellow group. This could possibly be attributed to the averaging effect the technique creates.

This study is intended to be indicative of the performance of the 2D Coherence Factor, and it does indeed seem that this tool could be beneficial to implement in ultrasound scanners. A larger study is needed, but the preliminary evidence does suggest that there are many positive benefits to the 2D Coherence Factor.

6.1   Future Work

The results in this paper are indicative of an increased image quality and resolution when the 2D Coherence Factor is applied. A number of other trends in the behaviour of the data have been found. In order to establish whether these trends are representative or circumstantial, a larger study of the 2D Coherence Factor is needed. Two main components in this next study are vital. The first is the size of the database. 45 videos from 9 patients were analyzed in this paper. In a larger study it is very important to have a larger amount of data. This would mean that any results would be more trustworthy, as the statistics are relevant for a larger portion of data. The second is the method in which the images and videos were analyzed. It is important that more than one person judges the ultrasound images, preferably clinicians that are familiar with echocardiography. These clinicians would need to compare the images from patients without knowing which image is from the 2D Coherence Factor. It is also important that the clinicians judging the images do not know the verdicts from the other clinicians in the study. It would also be beneficial if some kind of quantitative measurement on the performance of the algorithm could be established. This would make comparisons even simpler and more accurate.

In addition to this, it could be possible to look into the row-based nature of the algorithm. Perhaps it could be advantageous to have a column-based approach, or possibly combine the two into a process that can pick out coherence variations in both directions simultaneously.

References

[1] Tranquart, F., Grenier, N. Clinical use of ultrasound tissue harmonic imaging. 1999.

[2] Toulemonde, M. New beamforming strategy for improved ultrasound imaging : application to biological tissues nonlinear imaging. 2014.

[3] Fatemi, A., Måsøy, S. Row-based coherence imaging using a 2D-array transducer. 1994.

[4] Fatemi, A., Berg, EAR. Studying the origin of reverberation clutter in echocardiography: In vitro experiments and in vivo demonstrations. 2019.

[5] USTB Abstract. http://www.ustb.no/ius2017-abstract/. Accessed: 2020-04-28.

[6] Cardiovascular Disease. https://www.who.int/health-topics/cardiovascular-diseases/#tab=tab_1. Accessed: 2020-02-05.

[7] WHO: The Future of CVD. https://www.who.int/cardiovascular_diseases/en/cvd_atlas_25_future.pdf?ua=1. Accessed: 2020-02-05.

[8] Alizadehasl A. Sadeghpour, A. *Practical Cardiology*. Elsevier, 2018.

[9] Thomas Szabo. *Diagnostic Ultrasound Imaging*. Academic Press, 2004.

[10] Chirillo, F., Pedrocco, A. Impact of harmonic imaging on transthoracic echocardiographic identification of infective endocarditis and its complications. 2004.

[11] Mallart, R., Fink, M. Adaptive focusing in scattering media through sound-speed inhomogenities: The van cittert zernike approach and focusing criterion. 2019.

[12] Li, P.C., Li, M.L. Adaptive imaging using the generalized coherence factor. 2003.

[13] Lediju, M., Trahey, G. Short-lag spatial coherence of backscattered echoes: Imaging characteristics. 2011.

[14] Lediju, M., Goswami, R. Short-lag spatial coherence (slsc) imaging of cardiac ultrasound data: Initial clinical results. 2011.

[15] Camacho, J., Parrilla, M. Phase coherence imaging. 2009.

[16] Sletten, L. Patient Adaptive Imaging in Echocardiography: Coherence-based weighting for sidelobe suppression. 2019.

[17] Støylen, A. Basic Ultrasound for Clinicians. 2016.

[18] Piezoelectricity. https://en.wikipedia.org/wiki/Piezoelectricity.

[19] Hykes D. Starchman D. Hedrick, W. *Ultrasound Physics and Instrumentation*. Elsevier, 2005.

[20] Ultrasound Instrumentation, howpublished = http://folk.ntnu.no/thomg/TTK13/content-exercises. Accessed: 2019-12-14.

[21] Hillis, G., Bloomfield, P. Basic transthoracic echocardiography. 2005.

[22] Maleki, M., Esmaeilzadeh, M. The evolutionary development of echocardiography. 2012.

[23] Stanford Health Care: Different Types of Echocardiogram . https://stanfordhealthcare. org/medical-tests/e/echocardiogram/types.html. Accessed: 2020-05-06.

[24] Medical News Today. The heart: All you need to know . https://www.medicalnewstoday. com/articles/320565. Accessed: 2020-05-06.

[25] Anvari, A., Forsberg, F., Samir, A. A primer on the physical principles of tissue harmonic imaging. 2015.

[26] Hou, L., Liu, D. A filtering based scan converting method in ultrasound system. 2007.

[27] Rodriquez-Molares, A., Rindal, O. M. The ultrasound toolbox. 2017.

[28] MIPAV: Histogram Matching. https://mipav.cit.nih.gov/pubwiki/index.php/ Histogram_Matching. Accessed: 2020-05-04.

[29] Rindal, O.M., Rodriguez-Molares, A., Austeng, A. The dark region artifact in adaptive ultrasound beamforming. 2017.